Phase diagram of quasi-static immiscible displacement in disordered porous media

Ran Hu[1,2,†], **Tian Lan**[1,2], **Guan-Ju Wei**[1,2] **and Yi-Feng Chen**[1,2,†]

[1]State Key Laboratory of Water Resources and Hydropower Engineering Science, Wuhan University, Wuhan 430072, PR China

[2]Key Laboratory of Rock Mechanics in Hydraulic Structural Engineering of the Ministry of Education, Wuhan University, Wuhan 430072, PR China

Immiscible displacement in porous media is common in many practical applications. Under quasi-static conditions, the process is significantly affected by disorder of the porous media and the wettability of the pore surface. Previous studies have focused on wettability effects, but the impact of the interplay between disorder and contact angle is not well understood. Here, we combine microfluidic experiments and pore-scale simulations with theoretical analysis to study the impact of disorder on the quasi-static displacement from weak imbibition to strong drainage. We define the probability of overlap to link the menisci advancements to displacement patterns, and derive a theoretical model to describe the lower and upper bounds of the cross-over zone between compact displacement and capillary fingering for porous media with arbitrary flow geometry at a given disorder. The phase diagram predicted by the theoretical model shows that the cross-over zone, in terms of contact angle range, expands as the disorder increases. The diagram further identifies four zones to elucidate that the impact of disorder depends on wettability. In zone I, increasing disorder destabilizes the patterns, and in zone II, a stabilizing effect plays a role, which is less significant than that in zone I. In the other two zones, invasion morphologies are compact and fingering, respectively, independent of both contact angle and disorder. We evaluate the proposed diagram using pore-scale simulations, experiments in this work and in the literature, confirming that the diagram can capture the effect of disorder on displacement under different wetting conditions. Our work extends the classical phase diagrams and is also of practical significance for engineering applications.

Key words: porous media, microfluidics, capillary flows

---

1. Introduction

Fluid invasion into porous media to displace another immiscible fluid is an important process in many practical applications, such as enhanced oil recovery (Morrow & Mason 2001), geological carbon sequestration (Benson & Cole 2008), groundwater contamination by non-aqueous liquids (Dawson & Roberts 1997) and the design of fuel cells and microfluidic devices (Chapuis *et al.* 2008; Anderson, Zhang

† Email addresses for correspondence: whuran@whu.edu.cn, csyfchen@whu.edu.cn

& Ding 2010; Lee *et al.* 2017). For such flow behaviour of multiple fluids with an interface in porous media, the instability of the displacement front directly impacts the oil recovery efficiency, the CO_2 storage capacity and the rate of mass transfer between phases. In enhanced oil recovery, due to the unstable water–oil displacement front, water-flooding in natural reservoirs can produce only 10 %–20 % of the initial oil in place (Van't Veld & Phillips 2010). In geological CO_2 sequestration, when the injection of liquid CO_2 stops and brine flows back to displace supercritical CO_2, the occurrence of fingering flow can significantly increase the efficiency of storage by increasing interfacial area and improving capillary trapping as well as dissolution trapping (Wang *et al.* 2012; Bachu 2015). Understanding and controlling the immiscible fluid–fluid displacement in porous media is therefore critical for optimizing fluid management.

The instability of the displacement front is a classic problem and continues to be the focus of an enormous number of experimental, theoretical and numerical studies over the past five decades (Saffman & Taylor 1958; Paterson 1981; Måløy, Feder & Jøssang 1985; Lenormand, Touboul & Zarcone 1988; Dvraam & Payatakes 1995; Babchin *et al.* 2008; Cottin, Bodiguel & Colin 2011; Armstrong & Berg 2013; Bischofberger, Ramachandran & Nagel 2014; Hu *et al.* 2017*b*, 2018*b*; Singh *et al.* 2017; Rabbani *et al.* 2018). When gravity can be neglected, the competition between capillarity and viscous force controls the instability of the displacement front, which results in the patterns ranging from capillary fingering to viscous fingering to compact displacement (Lenormand *et al.* 1988; Zhang *et al.* 2011; Chen *et al.* 2017, 2018). This competing effect becomes more complicated when the wettability and the disorder of porous media are both involved (Alava, Dubé & Rost 2004; Singh *et al.* 2019). The wettability, denoted by the invading fluid contact angle θ, represents the affinity of fluid to the pore surface, which directly modifies the local pore-filling events via changing capillary force governed by the Young–Laplace law (Lenormand, Zarcone & Sarr 1983; Zacharoudiou *et al.* 2017) and thus impacts the overall displacement patterns (Cieplak & Robbins 1988; Holtzman & Segre 2015). On the other hand, the pore-scale disorder, λ, which represents the degree of randomness of pore size (Chen & Wilkinson 1985), would also impact the local pore-filling paths via changing the threshold capillary force that needs to be overcome by the pressure drop. Therefore, the challenge in characterizing the competition between disorder and wettability on the displacement patterns in porous media is how to link the pore-filling events that highly depend upon capillary force to the non-local invasion behaviour.

To unravel the fundamentals of fluid–fluid displacement processes in disordered porous media under various wetting conditions, theoretical and experimental studies have been conducted and are still on-going (Cieplak & Robbins 1988, 1990; Hecht & Taitelbaum 2004; Cottin *et al.* 2011; Holtzman & Segre 2015; Trojer, Szulczewski & Juanes 2015; Jung *et al.* 2016; Singh *et al.* 2017; Hu *et al.* 2018*a*). The pioneering work that links the pore-filling events to the non-local fluid invasion was proposed by Cieplak & Robbins (1988, 1990). They proposed three meniscus-motion modes (burst, touch and overlap), able to satisfactorily capture the pore-scale fluid displacement, to elucidate the wettability effect in disordered media, which are now widely recognized (Jung *et al.* 2016; Singh *et al.* 2017). These works provide a basic understanding of the wettability effect: namely that, as the pore surface becomes more wetting to the invading fluid within the range of $45° < \theta < 180°$, the displacement pattern becomes more stable. The critical contact angle θ_c that separates the unstable from the stable flow regimes is found to depend upon the porosity of the porous medium and the

capillary number (Cieplak & Robbins 1988; Hu *et al.* 2018*a*). Given the coexisting influence of wettability and disorder on local fluid displacement, this wettability effect should vary with disorder; for instance, the critical contact angle θ_c varies with disorder λ.

Although intensive research has focused on the effect of wettability on fluid displacement, less progress has been made in examining how the competition between pore-scale disorder and wettability controls the multiphase flow. In cases where the wettability effect is isolated, previous studies have shown that decreasing disorder stabilizes the displacement for both drainage and imbibition (Chen & Wilkinson 1985; King 1987; Toussaint *et al.* 2005) and that the disorder also modifies the critical capillary number Ca_c corresponding to the cross-over from capillary to viscous fingering (Yortsos, Xu & Salin 1997; Holtzman & Juanes 2010; Xu *et al.* 2014; Liu, Zhang & Valocchi 2015*b*). Recently, a systematic study on the impact of disorder and its coupling with wettability was conducted by Holtzman (2016). Based on scaling analysis, Holtzman (2016) introduced a capillary number Ca^* dependent on disorder and contact angle to consider the competition between disorder and wettability effect, showing that the critical capillary number Ca^* decreases with increasing λ for the range of $Ca > 10^{-5}$. Holtzman (2016) also showed that in the slowest flow rate considered ($Ca \approx 10^{-5}$), higher disorder of the flow geometry would enhance overlap events that smooth the local fluid–fluid interface, which is counter to the widely recognized effect that higher disorder destabilizes displacement patterns (Koiller, Ji & Robbins 1992). Given that, in the limit of quasi-static conditions, multiphase flow is significantly affected by the flow geometry, these counteracting effects that stabilize or destabilize would be amplified. Therefore, how the disorder impacts the quasi-static displacement pattern depends on which one of these counteracting effects is dominant. These effects can be clearly represented in a phase diagram in the $\theta-\lambda$ plane, which has not yet been reported.

Here, we aim to propose a phase diagram of quasi-static fluid displacement to elucidate how the competing effects between disorder and wettability control the fluid invasion pattern in porous media. It remains a great challenge to propose such a phase diagram because the number of arrangements of posts (or flow geometry) within disordered porous media can be infinite for any given disorder λ, because the radius of posts r_i can take any values following an assumed probability distribution, such as $r_i \sim U[(1 - \lambda)\bar{r}, (1 + \lambda)\bar{r}]$, where U denotes the uniform distribution, $\bar{r}$ is a constant and λ is the disorder of the porous medium (Chen & Wilkinson 1985; Holtzman & Segre 2015). For the classic and widely used phase diagram (Lenormand *et al.* 1988), the boundaries that separate the different flow regimes can be uniquely determined from the given flow rate and fluid properties within a specific flow geometry. However, because of the infinite flow geometries, the lower and upper bounds, rather than the specific boundaries, are established to separate the different flow regimes in the $\theta-\lambda$ plane. The zone bounded by the lower and upper limits provides the first identification of displacement patterns. This is very important because the statistical parameters, such as porosity, average particle/pore sizes and disorder, etc., are always easy to obtain for porous media. The flow regimes can then be easily determined via our phase diagram using these statistical parameters rather than the details of pore structure, which are difficult to obtain.

We combine microfluidic experiments, numerical simulations and theoretical analysis to describe the displacement patterns as a function of disorder and contact angle. We fabricate microfluidic chips with four different disorders and image the fluid displacement under extremely slow flow conditions with a microscope and a
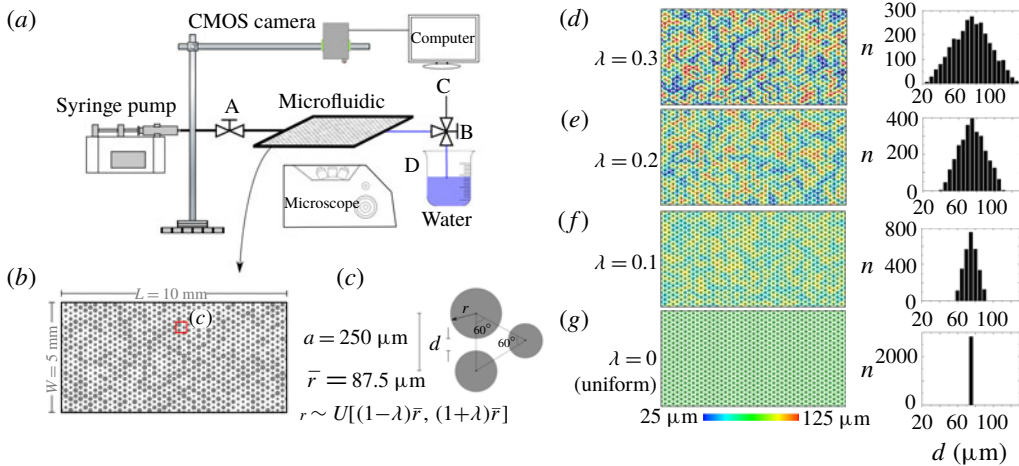
FIGURE 1. (Colour online) Microfluidic experimental set-up. (*a*) Schematic diagram of the microfluidic–microscopy system. (*b,c*) The flow geometry of the microfluidics is constructed by placing non-overlapping and variable-sized posts (r_i) on a triangular lattice with a spacing $a = 250$ µm, composed of 987 posts. The radii of the posts follow a uniform distribution. The length (L), width (W) and depth (D_0) of the microfluidics are, respectively, 10 mm, 5 mm and 40 µm. (*d–g*) Four microfluidics set-ups are fabricated with disorder $\lambda = 0$, 0.1, 0.2 and 0.3. The throat size distributions of the flow geometries with four disorders are, respectively, presented on the right side of panels (*d–g*). The porosity ϕ and the average throat size $\bar{d}$ for all of the microfluidics are nearly the same, i.e. $\phi = 0.55$ and $\bar{d} = 75$ µm.

complementary metal oxide semiconductor (CMOS) camera (§ 2.1). We develop a pore-scale numerical procedure originally proposed by Cieplak & Robbins (1988, 1990) to consider the rectangular geometry and constant-flow-rate conditions (§ 2.2). Based on experimental observations and numerical simulations (§ 3.1), we determine the flow regimes in the θ–λ plane for the flow geometries of the microfluidic chips (§ 3.2). Further, from the viewpoint of probability (§ 3.3.1), we derive a theoretical model that corresponds to the lower and upper bounds of flow regimes, and then propose a phase diagram in terms of disorder and wettability (§ 3.3.2). Finally, the proposed phase diagram is evaluated by extensive numerical simulations, our microfluidic experiments and other existing experimental results (§ 3.3.3).

2. Materials and methods

2.1. *Experimental section*

2.1.1. *Microfluidic visualization system*

We designed a microfluidic visualization system to perform fluid displacement experiments (figure 1*a*). The experimental set-up consists of a microfluidic flow cell, an imaging system and a syringe pump (Harvard Apparatus 70C3007). The syringe pump is used to control the flow rate. The imaging system, connecting to a computer, consists of an inverted microscope (Carl Zeiss, Observer Z1.m) that records images at the pore scale via a charge-coupled device (CCD) camera (Carl Zeiss, AxioCam MRc5), and a CMOS camera (Manta G-1236C, AVT) to record images of the entire domain of the microfluidics with a spatial resolution

of 39.0 μm pixel^{-1}. The microscope includes a reflecting light objective (Epiplan 5×/0.13 W0.8″, working distance = 20.5 mm) to visualize the fluid distribution within the range of 1.5 mm × 1.2 mm with a spatial resolution of 2.0 μm pixel^{-1}. The entire experimental set-up is maintained at room temperature (20 ± 0.5 °C).

2.1.2. *Microfluidic fabrication*

We fabricate the microfluidics with polydimethylsiloxane (PDMS) (Sylgard 184, Dow-Corning, USA). First, we construct the flow geometry of the microfluidics by placing non-overlapping and variable-sized posts on a triangular lattice with a spacing $a = 250$ μm (figure 1b,c). The post radius r_i follows a uniform distribution $r_i \sim U[(1 - \lambda)\bar{r}, (1 + \lambda)\bar{r}]$, where $\bar{r}$ is the average radius, $\bar{r} = 87.5$ μm. The manufacturing resolution is 1 μm, and thus the roughness of post surfaces is approximately 1 μm. Four flow geometries are generated with $\lambda = 0, 0.1, 0.2$ and 0.3 (figure 1d–g). Then, we generate the corresponding silicon masters using conventional photolithography techniques, including (1) spin-coating a negative photoresist (SU8-2035, MicroChem, USA) to achieve a film thickness of 40 μm onto a 4″ silicon wafer at 2000 revolutions per minute for 30 s, and (2) exposing the photoresist to ultraviolet (UV) light with a photomask to generate the patterned silicon master. Finally, we obtain a PDMS patterned plate by pouring PDMS onto the silicon master, and then create a microfluidic flow cell by bonding this PDMS patterned plate with a smooth PDMS plate using a Plasma Cleaner (PDC-002, Harrick Plasma, USA). Four different patterns of microfluidics (figure 1d–g), composed of 987 posts, are generated. The pore volumes (*PV*) of the four microfluidics are almost the same, $PV = 1.1$ μl, and the porosity is $\phi = 0.55$. We calculate the spatial correlation length of the flow geometry. Since the posts are located on triangular lattices, the correlation lengths for the microfluidics are the same, i.e. $l_c = 1.3a$.

2.1.3. *Experimental procedure*

Given that the pore surface of microfluidics is hydrophobic, for the purpose of imbibition experiments using the water–air fluid pair, the invading fluid of air is the wetting phase and the degassed water is the defending (non-wetting) phase. We measure the contact angle between water and air on the smooth PDMS plate with a Drop Shape Analyzer (DSA25; Krüss), and the average invading fluid (air) contact angle is $\theta = 67°$. The water is dyed with a light-absorbing dye (Carmine, Wilton) at 0.2 wt.% concentration to increase the signal intensity between the two phases. To conduct a weak imbibition experiment, we first fully saturate the microfluidic with the withdraw mode of the syringe pump at a constant flow rate of 1 μl min^{-1} via the flow path D → B → A for 5 min (figure 1a). Afterwards, the three-way valve B is switched to C, and the system is equilibrated at 20 °C for 15 min. After that, imbibition processes are initiated. Air is injected into the microfluidic at the extremely slow flow rate of 0.025 μl min^{-1} with the withdraw mode of the pump via the flow path C → B → A. Images of invasion morphology for the entire domain of the microfluidic are recorded at 10 frames min^{-1} with the CMOS camera until the invading fluid reaches the outlet. Higher-resolution images of fluid distributions at the pore scale are also recorded with the microscope. The above procedures are applied to the microfluidics with $\lambda = 0, 0.1, 0.2$ and 0.3, and each disorder condition is repeated four times, with a total of 16 imbibition experiments. Each microfluidic is used only for one time. The procedure for image post-processing has been reported in the previous study (Hu *et al.* 2017b). To confirm that the flow-rate condition corresponds to the quasi-static state, we calculate the capillary number *Ca*, which is

widely used to quantify the relative effect of viscous to capillary forces (Lenormand *et al.* 1988; Zhang *et al.* 2011; Chaudhary *et al.* 2013; Geistlinger *et al.* 2015). Here, Ca is calculated by $Ca = v_i \mu_i / \sigma$, where $v_i = Q/A_c$, $Q = 0.025 \ \mu l \ min^{-1}$, A_c is the cross-sectional area of the inlet, $A_c = W \times D_0 = 5 \ mm \times 40 \ \mu m$ (figure 1*b*), $\mu_i = 1.83 \times 10^{-5} \ kg \ m^{-1} \ s^{-1}$ and $\sigma = 7.25 \times 10^{-2} \ N \ m^{-1}$. Thus, the capillary number under such flow-rate conditions is $Ca = 4.2 \times 10^{-10}$, which generally corresponds to the quasi-static condition.

2.2. *Numerical simulation*

We develop the model of Cieplak & Robbins (1988, 1990) to simulate the quasi-static fluid–fluid displacement processes, starting with the basic modes for menisci motion in §2.2.1 and the numerical implementation in §2.2.2.

2.2.1. *Modes for menisci motion*

Cieplak & Robbins (1988, 1990) introduced three basic modes for menisci motion, i.e. burst, touch and overlap. These modes, able to capture the local fluid displacement, are fundamental to the pore-scale numerical simulation for fluid inversion into porous media, and also the basis for the derivation of the phase diagram in this work. From geometry analysis, we can obtain the onsets of burst, touch and overlap for non-uniform post arrangements.

The burst event occurs when no stable arc can exist in the current post arrangement with contact angle and local pressure drop. As the local pressure drop increases, the radius of curvature decreases. Once the radius of curvature reaches its minimum, an infinitesimal increment of pressure drop would cause the invading fluid to burst into the adjacent pores, also known as Haines jump (Berg *et al.* 2013). Thus, the critical radius of curvature, R_b, for the occurrence of the burst mode corresponds to its minimum. As shown in figure 2(*a*), based on geometry analysis (see §A.1), we have

$$\text{burst:} \quad R_b = \frac{-b_1 + \sqrt{b_1^2 - 4a_1 c_1}}{2a_1}, \tag{2.1}$$

where a_1, b_1 and c_1 are the coefficients given in table 1 and (A 3).

For the touch event, the radius of curvature continues to decrease and then touches the edge of the nearest post before reaching its minimum (figure 2*b*). Again, based on geometry analysis on figure 2(*b*) (see §A.2), the condition for the occurrence of touch is given as

$$\text{touch:} \quad R_t = \frac{-b_2 + \sqrt{b_2^2 - 4a_2 c_2}}{2a_2}, \tag{2.2}$$

where a_2, b_2 and c_2 are the coefficients given in table 1 and (A 6).

Note that during numerical simulation, one needs to identify which mode occurs first. Hecht & Taitelbaum (2004) showed that the effect of the order of occurrence for the three basic modes on the multiphase flow is not very important. Holtzman & Segre (2015) check for the burst first and then check for the touch and overlap events, which is employed in this study. As shown in figure 2(*c*), we consider a specific fluid reconfiguration in which the point A is located on $O_1 O_2$ and the arc BC touches the nearest post, indicating that there is a critical radius of curvature corresponding to the two modes. To determine the order of occurrence of the two modes, we determine the critical radius R_c,

$$R_c = \sqrt{\tfrac{1}{2}a^2 + \tfrac{1}{2}(r_1^2 + r_2^2) + R_b^2 - (r_1 + r_2)R_b \cos\theta} - r_3, \tag{2.3}$$
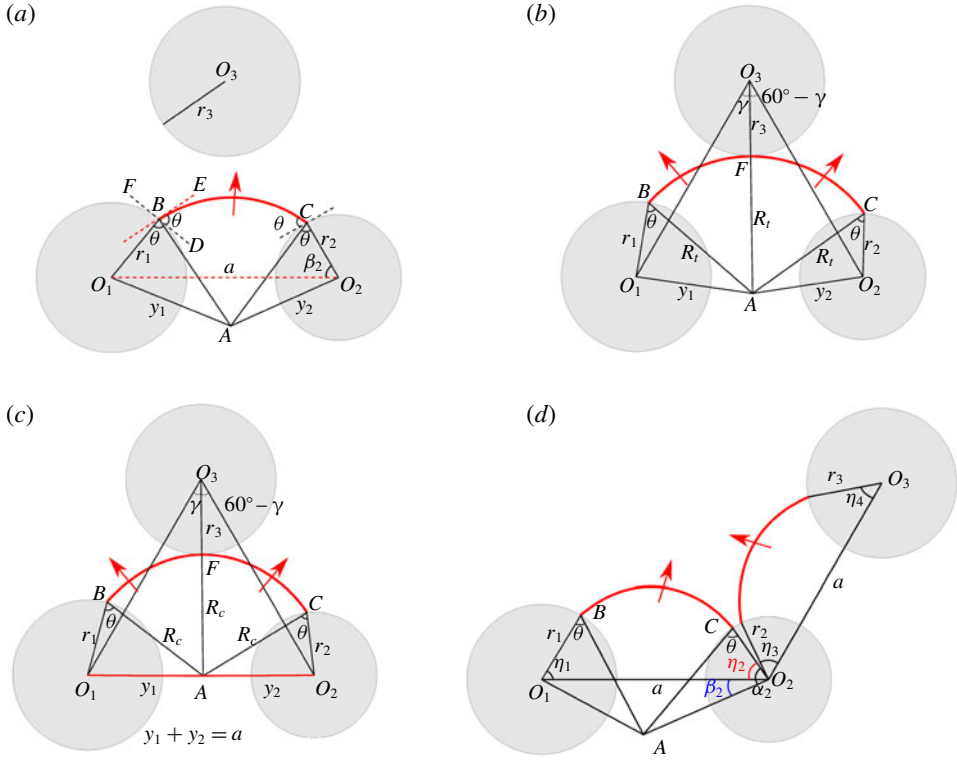
FIGURE 2. (Colour online) The geometry to calculate to radii of curvature of the menisci for the three basic modes as introduced by Cieplak & Robbins (1988). (*a*) Burst. The onset of a burst event corresponds to the state that for the minimum radius of curvature (the maximum capillary force) no stable meniscus can exist in such an arrangement of the posts. (*b*) Touch. The occurrence of touch means that the meniscus has touched the edge of the nearest post before the radius of curvature reaches its minimum. (*c*) The order of occurrence for burst and touch before determining overlap. (*d*) Overlap. Two menisci merge into one at the location of the three-phase contact line. The arrow indicates the direction of menisci motion, and the red arc indicates the fluid–fluid interface.

where R_b is the critical radius given by (2.1). If $R_b < R_c$, then the burst has occurred before the arc has touched the nearest post (touch). Conversely, if $R_b > R_c$, then the touch has occurred before the burst.

The overlap mode involves two neighbouring menisci merging into a new one at the three-phase contact point or at the fluid–fluid interface (Primkulov *et al.* 2018; Singh *et al.* 2019). Primkulov *et al.* (2018) have shown that for larger post–post spacing with $\theta \geqslant 110°$, the percentage of overlap events will be underestimated when considering the two menisci merging at the three-phase contact point. We check the two treatments, and the results show that the difference in the probability of overlap (see (3.3)) is no more than 0.05. Here, as shown in figure 2(*d*), we consider the former case that is widely used (Koiller *et al.* 1992; Holtzman & Segre 2015). For this post arrangement, the overlap will occur if $\eta_2 + \eta_3 \geqslant \angle O_1 O_2 O_3$. Through geometry analysis (see § A.3), we have the condition

$$\text{overlap:} \quad \eta_2(r_1, r_2, R, \theta) + \eta_3(r_2, r_3, R, \theta) \geqslant \phi_0, \tag{2.4}$$

Modes	Coefficients

	$a_1 = \dfrac{2}{a^2}(r_1 - r_2)^2 \cos^2\theta - 2$
Burst	$b_1 = 2(r_1 + r_2)\cos\theta - \dfrac{2}{a^2}(r_1 - r_2)^2(r_1 + r_2)\cos\theta$
	$c_1 = \dfrac{a^2}{2} + \dfrac{1}{2a^2}(r_1^2 - r_2^2)^2 - r_1^2 - r_2^2$

$$a_2 = 4r_3^2 + 4\cos^2\theta(r_1^2 + r_2^2 - 4r_1 r_3) + 4r_3\cos\theta(r_2 + r_1) - 3a^2$$

Touch
$$b_2 = 2a^2(r_1\cos\theta + r_2\cos\theta - 2r_3) + 2r_1\cos\theta(r_2^2 + r_3^2 - 2r_1^2)$$
$$+ 2r_2\cos\theta(r_1^2 + r_3^2 - 2r_2^2) + 2r_3(2r_3^2 - r_1^2 - r_2^2)$$

$$c_2 = a^2(a^2 - r_1^2 - r_2^2 - r_3^2) + \tfrac{1}{2}(r_1^2 - r_2^2)^2 + \tfrac{1}{2}(r_1^2 - r_3^2)^2 + \tfrac{1}{2}(r_2^2 - r_3^2)^2$$

Overlap
$$\eta_2 = \cos^{-1}\left(\frac{r_2 - R\cos\theta}{\sqrt{r_2^2 + R^2 - 2r_2 R\cos\theta}}\right) - \cos^{-1}\left(\frac{a^2 + r_2^2 - r_1^2 + 2(r_1 - r_2)\cos\theta}{2a\sqrt{r_2^2 + R^2 - 2r_2 R\cos\theta}}\right)$$

$$\eta_3 = \cos^{-1}\left(\frac{r_2 - R\cos\theta}{\sqrt{r_2^2 + R^2 - 2r_2 R\cos\theta}}\right) - \cos^{-1}\left(\frac{a^2 + r_2^2 - r_3^2 + 2(r_3 - r_2)\cos\theta}{2a\sqrt{r_2^2 + R^2 - 2r_2 R\cos\theta}}\right)$$

TABLE 1. Coefficients in (2.1), (2.2) and (2.4).

where the expressions for η_2 and η_3 are given in table 1 and (A 11)–(A 12), and R is the radius of curvature for the burst or touch, depending on which mode occurs first. If the burst occurs first, i.e. if $R_b < R_c$, then $R = R_b$; while if $R_b > R_c$, then $R = R_t$, and ϕ_0 is the angle of $\angle O_1 O_2 O_3$. For the triangular lattice considered in this work (figure 1c), ϕ_0 is set as $120°$.

2.2.2. *Numerical implementation*

We develop the method of Cieplak & Robbins (1988, 1990) to consider a rectangular domain with constant-flow-rate condition, different from the previous modes, which are applicable for a circular domain and constant-pressure conditions (Cieplak & Robbins 1990; Koiller *et al.* 1992). To reproduce the observed quasi-static fluid displacement, we create an irregular rectangular two-dimensional (2-D) model for the microfluidics (figure 1d–g). The inlet (the left side of figure 1b) is fixed with a constant flow rate of $Q_0 = 0.025$ µl min^{-1}, and zero pressure and no-flow conditions are, respectively, applied on the outlet (the right side) and the lateral boundaries (the top and bottom sides). First, all of the pores are saturated with the defending fluid, and the two rows of pores near the inlet are filled with the invading fluid. Then, the Stokes-flow-based continuity equation is assembled for the system, i.e. $Q = KP$, where Q is the vector of flux into the pores, P is the vector of pressure for each pore, and K is the matrix that represents the conductance for adjacent pores of the system. After solving the equation, i.e. $P = K^{-1}Q$, the pressure for each pore is updated, and thus the radius of curvature for all arcs. After that, the local pore-filling events, i.e. burst, touch and overlap, are identified with (2.1), (2.2) and (2.4), to update the configuration of menisci. Once the menisci advancements have been tracked, the conductance for adjacent throats, K, is updated. Through repeating the above procedure until one meniscus reaches the outlet, we can simulate the quasi-static fluid invasion processes

in porous media. More details of the numerical implementation can be found in the existing works (Holtzman & Segre 2015; Holtzman 2016).

Since the numerical method is developed for the 2-D system (figure 2), the fluid advancements with three-dimensional (3-D) nature and the related mechanisms of corner flow (Dong & Chatzis 1995; Weislogel & Lichter 1998), snap-off (Roof 1970) and spreading of thin wetting films (Levaché & Bartolo 2014; Odier *et al.* 2017) cannot be considered in numerical simulations. These important mechanisms would dominate the displacement in the case of strong imbibition such as $\theta < 45°$ (Concus & Finn 1969) or in the case of relatively high flow rate (Zhao, MacMinn & Juanes 2016; Hu *et al.* 2018*a*). However, for the cases of quasi-static fluid displacement in the range of $\theta > 45°$ considered in this work, the numerical model based on Cieplak & Robbins (1988, 1990) is adequate for capturing the fluid invasion processes. The advantage of the employed numerical model is its high computational efficiency compared with other direct simulation techniques, such as the computational fluid dynamics (CFD) method (Ferrari *et al.* 2015; Hu *et al.* 2017*a*) and lattice Boltzmann method (LBM) (Liu *et al.* 2015*a*). For CFD and LBM, it is extremely expensive, requiring parallel computing lasting for several weeks with 24–95 processors in clusters (Raeini, Bijeljic & Blunt 2015), for simulating such quasi-static fluid displacement. The high efficiency of the numerical method used in this work enables us to systematically investigate the fluid displacement over a wide range of parameters that are difficult to achieve in experiments.

3. Results and discussion

3.1. *Impact of disorder on displacement patterns for weak imbibition*

Figure 3 presents the observed and simulated displacement patterns in the case of weak imbibition ($\theta = 67°$) from the initial state to the breakthrough time. The experimental results (figure 3*a*,*c*,*e*,*g*) demonstrate that increasing disorder λ destabilizes the immiscible two-phase flow. For uniform porous media (figure 3*g*), a compact displacement is observed, but the front gradually becomes unstable as λ increases. The destabilizing effect of the disorder can also be confirmed in terms of the variations of the invading fluid saturation at the breakthrough time S_{br} (figure 4*a*) and the specific fluid–fluid interface length l_{nw} (figure 4*b*), where l_{nw} is defined by the length of displacement front divided by the average pore throat, excluding the trapped regions behind the front. As shown in figure 4, the measured saturation S_{br} decreases with the disorder λ, while the measured specific interface length l_{nw} increases with λ.

The simulated invasion morphologies, shown in figure 3(*b*,*d*,*f*,*h*), are generally consistent with the experimental results. Inspection of the local fluid distributions in the marked regions (figure 3*a*,*c*,*e*,*g*) shows that the defending phase is trapped within single or multiple pores. Although our numerical method is able to capture trapping in fluid displacement (see figure 9*d*,*e* in §3.3.3), the observed trapping behaviour in microfluidics is not reproduced via simulations. The discrepancy is mainly attributed to limited fabrication resolution, which induces roughness at the edges of posts of the scale of 1 µm. From the theory of multiphase flow, for weak imbibition ($\theta = 67°$) in uniform porous media under quasi-static conditions, all of the neighbouring menisci would merge and the driving front should be flat, leading to 100 % of the defending fluid being displaced, which can be well captured by the simulation (figure 3*h*). For the experiment with $\lambda = 0$ (figure 3*g*), due to manufacturing precision limits, slight changes in post thickness or radii introduce heterogeneity into a homogenous sample (Borgman *et al.* 2017), which determines the invasion path and finally induces
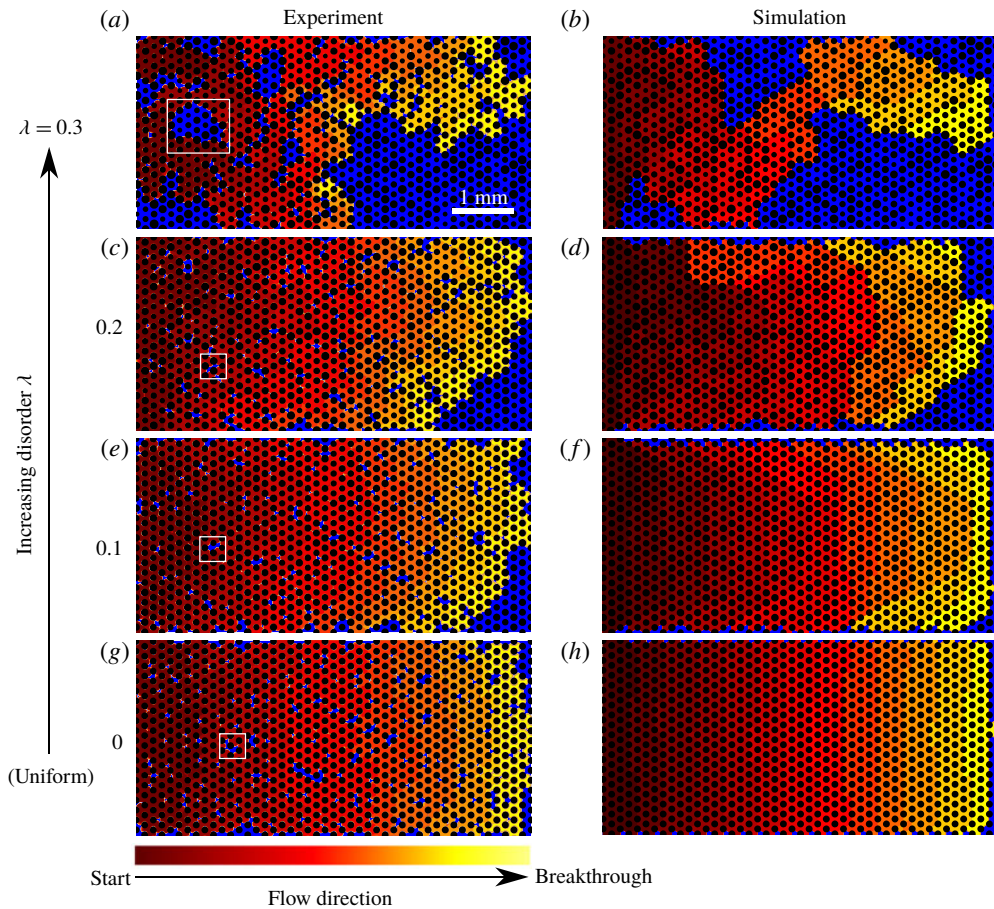
FIGURE 3. (Colour online) The observed (*a,c,e,g*) and simulated (*b,d,f,h*) invasion morphologies at the time of breakthrough when the invading fluid reaches the outlet of the microfluidic flow cell. The disorder λ increases from the bottom to top rows, with $\lambda = 0$ (*g,h*), $\lambda = 0.1$ (*e,f*), $\lambda = 0.2$ (*c,d*) and $\lambda = 0.3$ (*a,b*). The red colour is the invading phase and the blue colour is the defending phase. To show the evolution of the displacement front, the dark red represents the initial stage whereas the light red indicates the late time. There are 987 posts in the microfluidics used in the experiments and simulations. We isolate the effect of porosity ϕ, and the values of porosity for all microfluidics are nearly the same, i.e. $\phi = 0.55$.

trapping (Geistlinger *et al.* 2015). Therefore, in comparison with the experimental results (figure 4), higher saturation S_{br} and lower interface length l_{nw} are obtained in the simulation for $\lambda = 0$ and for the relatively uniform porous medium ($\lambda = 0.1$). The relative percentage errors of saturation and interface length are, respectively, 21.3 % and -21.6 % for $\lambda = 0$ and 21.8 % and -16.9 % for $\lambda = 0.1$. When λ increases up to 0.2 and 0.3, the simulated saturation S_{br} and interface length l_{nw} are closer to the measurements, with the relative percentage errors decreasing to 4.8 % and 5.2 % ($\lambda = 0.2$) and 5.2 % and 10.3 % ($\lambda = 0.3$). The reason is that, as previously indicated, for more highly disordered porous media, the disorder dominates the fluid invasion over the roughness of post edges at small scale.
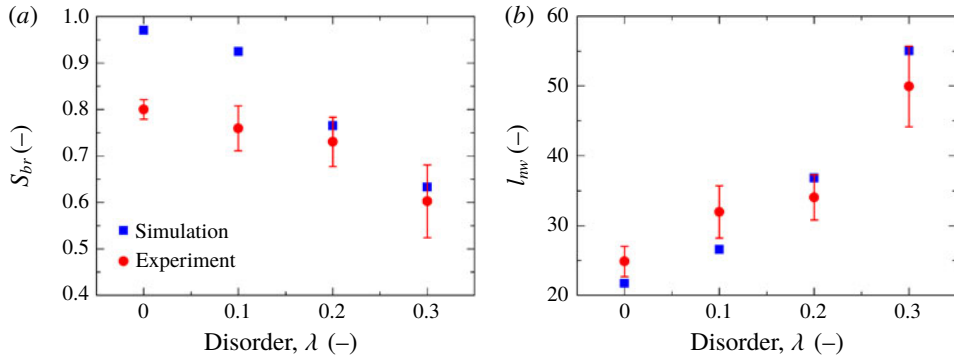
FIGURE 4. (Colour online) Comparison between experimentally measured and numerically simulated results for (*a*) the invading fluid saturation S_{br} and (*b*) the specific fluid–fluid interface length l_{nw} at the time of breakthrough for different disorders. For the measurements, the data points (solid circles) indicate the average values of four replicate experiments, and the error bars indicate standard deviations.

The trapping behaviour in disordered porous media can be reproduced with simulation in the case of $\lambda = 0.25$ and $\theta = 75°$ (see figure 9*d*) but cannot be reproduced in the disordered microfluidics used in experiments ($\lambda = 0.1$, 0.2, 0.3 and $\theta = 67°$), which means that systematic comparison of the trapped defending fluids between experiments and simulations under various disorders and wetting conditions needs to be conducted. Nevertheless, comparison between experiments and simulations mentioned above shows that the 2-D numerical simulations can generally reproduce the invasion morphology observed in the microfluidics and can capture the impact of disorder on quasi-static displacement patterns for weak imbibition.

3.2. *Link pore-filling events to displacement pattern*

The pore-scale fluid displacement directly determines the displacement patterns. To obtain further insight into the disorder effect, using the microscope we randomly select the fields of view in the microfluidics with $\lambda = 0$ and $\lambda = 0.3$, and record the pore-scale images for local fluid advancements. As shown in figure 5, we observe that, for uniform porous media, the menisci (labelled with 1 and 2) advance from t_1 to t_3 and finally merge into a single meniscus at t_4, known as overlap (see figure 2*d*), which stabilizes the fluid–fluid interface. In disordered media, however, the menisci (1 and 2) cannot merge, because r_4 is very large so that the meniscus 1 touches its edge and finally induces a volume of defending fluid to be trapped within the pore throat. Quantitatively, the observed coalescence of neighbouring menisci (figure 5*a*) suggests that the conditions for the occurrence of overlap expressed by (2.4) are satisfied in the uniform porous media with $\theta = 67°$, while this condition is not satisfied in the non-uniform post arrangement in figure 5(*b*). As the number of overlap events in the porous media increases, the displacement pattern becomes more stable.

To link the advancements of menisci to the displacement patterns, we calculate the probability of overlap, P_{ov}, by traversing through all of the post arrangements shown in figure 2(*d*). The probability, P_{ov}, is defined as $P_{ov} = N_{ov}/N$, where N_{ov} is the number of post arrangements for which the overlap event occurs ((2.4) is satisfied), and N is the total number of post arrangements. If $P_{ov} = 1$, overlap occurs for all of the post arrangements, indicating that the displacement is compact. For $P_{ov} = 0$, no overlap
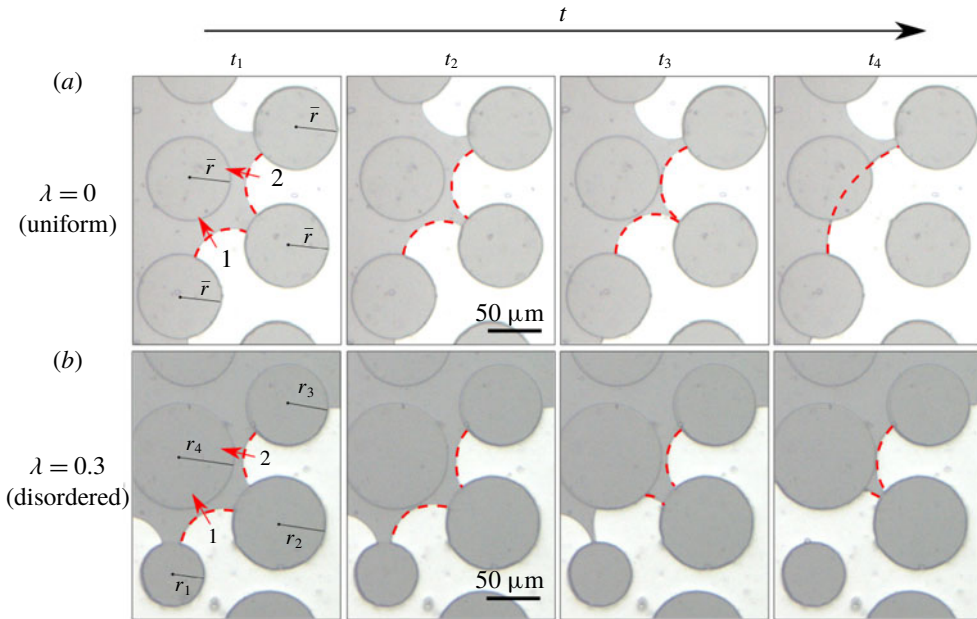
FIGURE 5. (Colour online) The pore-scale images for local fluid displacement with the inverted microscope in the (*a*) uniform and (*b*) disordered microfluidics at t_1, t_2, t_3 and t_4, where the time interval between t_2 and t_1, and between t_3 and t_2 is $\Delta t = t_3 - t_2 = t_2 - t_1 = 5$ min, and that between t_4 and t_3 is 50 s. The arrow indicates the direction of menisci motion and the red dashed line indicates the fluid–fluid interface. The light colour is the invading phase whereas the dark colour is the defending phase. The solid phase (posts) is also shown with dark colour but can be distinguished by its edge (circumference).

occurs and burst dominates the displacement, and the pattern is capillary fingering. For the cross-over between compact displacement and capillary fingering, $0 < P_{ov} < 1$. Thus, we relate the probability of overlap, P_{ov}, to the displacement patterns. Holtzman & Segre (2015) performed scaling analysis of viscous and capillary forces and found that the compact displacement only requires 40 %–50 % of overlap events, which is different from the threshold ($P_{ov} = 1$) in this work. This is due to the different definitions between the probability and the percentage for overlap events. In the work of Holtzman & Segre (2015), the percentage of overlap events is calculated by the ratio of the number of overlaps to all instability events determined from numerical simulations. However, in this work, the probability of overlap P_{ov} is determined from geometry analysis (without numerical simulations), which means that all of the post arrangements are considered even if some of them are not occupied by the invading fluid. Under quasi-static conditions where the fluid invasion is significantly affected by the geometry, this treatment is reasonable and the relationship between P_{ov} and displacement patterns will be evaluated in § 3.3.3. Recently, Wang *et al.* (2019) introduce an indicator, i.e. capillary index I_c, to represent the collaborative effect of disorder and wettability. Based on the variation of fluid–fluid interface length with the invading fluid saturation, they report that $I_c \geqslant 0.5$ corresponds to the stable displacement and fingering occurs for $I_c \leqslant 0.5$. Note that trapping of defending fluid is also important during the immiscible displacement and would significantly affect the displacement pattern/efficiency. However, under quasi-static displacement
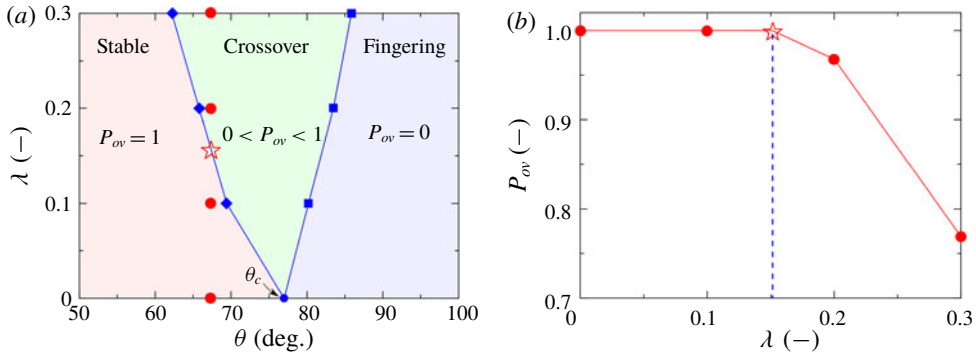
FIGURE 6. (Colour online) (*a*) The domains of capillary fingering, compact displacement and the cross-over between them in the θ–λ plane for four specific flow geometries with $\lambda = 0$, 0.1, 0.2 and 0.3. For each flow geometry, the blue diamonds are the critical contact angle below which the probability of overlap P_{ov} is 1.0, whereas the blue squares correspond to the critical contact angle above which the probability of overlap is 0. The red circles indicate the experimental conditions. (*b*) The variation of the probability of overlap P_{ov} with the disorder λ for the contact angle of pore surface of the microfluidics, i.e. $\theta = 67°$. The open red star in (*a*) and (*b*) indicates the points that separate the stable displacement and the cross-over when the disorder λ increases.

conditions, trapping is closely related to the probability of overlap, P_{ov}. When the dynamic effect is absent, smaller P_{ov} indicates a larger number of intermittent advancements of menisci at different locations, resulting in a larger trapped volume of the defending fluid (Holtzman & Segre 2015), and then destabilizes the displacement front. Therefore, the trapping is implicitly considered in our work.

By traversing through all of the post arrangements and checking the conditions of basic modes given by (2.1), (2.2) and (2.4), we calculate the variation of P_{ov} with contact angle θ ($45° < \theta < 180°$) for the four microfluidics with $\lambda = 0$, 0.1, 0.2 and 0.3. Then, we can obtain the critical contact angle below which P_{ov} is 1.0 (diamonds in figure 6*a*), and another critical contact angle above which P_{ov} is 0 (squares). Thus, as shown in figure 6(*a*), three zones of compact displacement ($P_{ov} = 1$), capillary fingering ($P_{ov} = 0$) and the cross-over between them ($0 < P_{ov} < 1$) are bounded by the two polylines constructed with these critical contact angles (diamonds and squares). The variation of P_{ov} with λ for the experimental conditions can also be directly obtained when θ is fixed as $67°$.

Figure 6(*a*) elucidates the impact of disorder not only in weak imbibition but also in the full range of drainage. Our experimental conditions in weak imbibition are also presented in figure 6 for a comparison purposes. As λ increases from 0 to 0.3, the displacement pattern shifts from compact displacement to the cross-over at the critical disorder ($\lambda = 0.151$). The observed destabilizing effect of disorder can be quantified by the probability P_{ov} (figure 6*b*). We observe that $P_{ov} = 1$ in the zone of compact displacement ($\lambda \leqslant 0.151$), and that P_{ov} decreases as $\lambda > 0.151$ for the cross-over. Figure 6(*a*) also shows that, for $\theta > \theta_c$, increasing disorder would stabilize the displacement patterns, and the underlying mechanism will be discussed in § 3.3.2.

3.3. *Phase diagram*

Section 3.2 demonstrates that the zones of different displacement patterns in the θ–λ plane are bounded by the contours of $P_{ov} = 1$ and $P_{ov} = 1$. The boundaries that separate

the different flow regimes are calculated based on the geometry analysis for specific flow geometry with a given λ (0, 0.1, 0.2 and 0.3). Given the infinite flow geometries for a given λ, there are infinite boundaries for displacement flow regimes. In this section, we derive a theoretical model for describing the lower and upper bounds for the compact displacement and capillary fingering in the $\theta-\lambda$ plane.

3.3.1. *Probability of overlap for an arbitrary geometry*

We first redefine the probability of overlap P_{ov} for an arbitrary geometry with a given λ. Since the radii of posts follow a uniform distribution, i.e. $r_i \sim U[(1-\lambda)\bar{r}, (1+\lambda)\bar{r}]$, the probability density function $f(r)$ for the uniform distribution is given by

$$f(r) = \begin{cases} \dfrac{1}{2\lambda\bar{r}}, & r \in [(1-\lambda)\bar{r}, (1+\lambda)\bar{r}], \\ 0, & \text{otherwise.} \end{cases} \quad (3.1)$$

Based on probability theory, the probability of picking a three-post arrangement (r_1, r_2 and r_3) out of the geometry with 987 posts for a given λ is

$$f_{123}(r_1, r_2, r_3) = \begin{cases} \dfrac{1}{(2\lambda\bar{r})^3}, & (r_1, r_2, r_3) \in G, \\ 0, & \text{otherwise,} \end{cases} \quad (3.2)$$

where G is a bounded closed region expressed by $G = \{(r_1, r_2, r_3); (1-\lambda)\bar{r} \leqslant r_i \leqslant (1-\lambda)\bar{r}, \; i = 1, 2, 3.\}$ with its volume being $(2\lambda\bar{r})^3$. According to the condition for the occurrence of overlap (2.4), the probability of overlap for an arbitrary geometry with a given λ can be written as

$$P_{ov} = \iiint_{G \cap G_{ov}} \frac{1}{(2\lambda\bar{r})^3} \, dr_1 \, dr_2 \, dr_3, \quad (3.3)$$

where G_{ov} is the region in which the overlap occurs, depending upon λ and θ, expressed by

$$G_{ov}(\lambda, \theta) = \{(r_1, r_2, r_3) : \eta_2(r_1, r_2, r_3; \lambda, \theta) + \eta_3(r_1, r_2, r_3; \lambda, \theta) \geqslant 2\pi/3\}, \quad (3.4)$$

where r_1, r_2, r_3 and η_2, η_3 are variables in the three-post arrangement shown in figure 2(*d*).

By (3.3), we calculate P_{ov} as a function of disorder and contact angle, as presented in figure 7(*a*). The contours of P_{ov} are employed to classify the different flow regimes for an arbitrary geometry with a given λ. Figure 7(*a*) shows that the flow regimes of compact displacement and capillary fingering are separated by the boundary curves of $\theta_{CD}(\lambda)$ and $\theta_{CF}(\lambda)$ in the $\theta-\lambda$ plane. The boundary curve $\theta_{CD}(\lambda)$ is the lower bound of the contact angles below which the probability of overlap P_{ov} is 1.0 (compact displacement), whereas the curve $\theta_{CF}(\lambda)$ corresponds to the upper bound of the contact angles above which the probability of overlap is 0 (capillary fingering). The area bounded by the two curves is the cross-over zone from capillary fingering to compact displacement. Thus, a phase diagram of the quasi-static fluid displacement pattern with disorder and contact angle can be straightforwardly established when the boundary curves are determined.
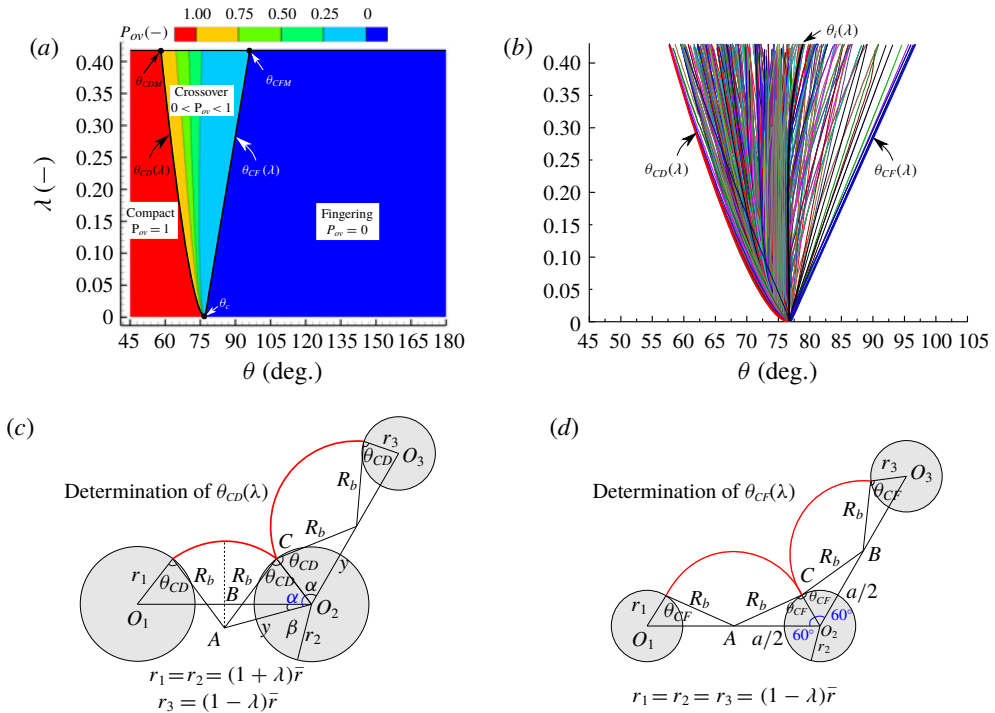
FIGURE 7. (Colour online) (*a*) Phase diagram of quasi-static immiscible displacement in the θ–λ plane with λ ranging from 0 to $\lambda_{max} = a/\bar{r} - 1$ (corresponding to the state of posts overlapping), and with θ ranging from 45° to 180°. The probability of overlap P_{ov} is presented with red colour for a higher value and with blue colour for a lower value. The probability of overlap P_{ov} as a function of θ and λ is used to classify the different displacement patterns, i.e. $P_{ov} = 1$ for stable displacement, $P_{ov} = 0$ for capillary fingering and $0 < P_{ov} < 1$ for the cross-over between them. The thick curves of $\theta_{CD}(\lambda)$ and $\theta_{CF}(\lambda)$ are the lower and upper bounds of the cross-over zone from capillary fingering to compact displacement. (*b*–*d*) Determination of the curves of $\theta_{CD}(\lambda)$ and $\theta_{CF}(\lambda)$. Each curve, $\theta_i(\lambda)$, corresponding to a post arrangement with constant ratios among the three radii, describes the critical θ below which no overlap occurs and above which burst occurs. Based on geometry analysis of sampling points, the curves $\theta_{CD}(\lambda)$ and $\theta_{CF}(\lambda)$, respectively, correspond to the post arrangements given in (*c*) and (*d*).

3.3.2. *Phase diagram*

To derive the analytical (or semi-analytical) solutions for the boundary curves of $\theta_{CD}(\lambda)$ and $\theta_{CF}(\lambda)$, we perform geometry analysis on a larger number of post arrangements according to the conditions of the occurrence of overlap (2.4). We consider 100×135 intervals in the θ–λ space of $[0, \lambda_{max}] \times [45°, 180°]$, and consider $100 \times 100 \times 100$ intervals for the bounded closed region G. Thus, a total of 1.35×10^{10} sampling post arrangements are analysed. Figure 7(*b*) presents a series of curves from geometry analysis. Each curve, $\theta_i(\lambda)$, corresponds to the critical contact angle for a post arrangement with constant ratios among the three radii. Below $\theta_i(\lambda)$ no overlap occurs and above it burst occurs. Thus, as shown in figure 7(*b*), the left envelope of these curves indicates that overlap unconditionally occurs in its left area, whereas overlap never occurs and burst dominates the displacement in the right side of the right envelope. The two envelopes have the same physical meanings as those of

$\theta_{CD}(\lambda)$ and $\theta_{CF}(\lambda)$ shown in figure 7(*a*). Interestingly, we find that the two envelopes respectively correspond to the two post arrangements given in figures 7(*c*) and 7(*d*), which can be used to derive analytical (or semi-analytical) solutions of $\theta_{CD}(\lambda)$ and $\theta_{CF}(\lambda)$.

For the boundary curve of $\theta_{CF}(\lambda)$, the related post arrangement (figure 7*d*) shows that the three radii reach their minimum and that the burst occurs for the two menisci. Based on geometry analysis (§ B.1), we derive the analytical solution for $\theta_{CF}(\lambda)$ as

$$\theta_{CF}(\lambda): \quad \lambda = 1 - \bar{l}^{-1}\left(\left[\frac{f_1(\theta)}{f_2(\theta)}\right]^2 + \frac{f_1(2\theta) - 3}{f_2(\theta)} + 1\right)^{-1/2}, \tag{3.5a}$$

with

$$f_1(\theta) = \sqrt{3}\sin\theta - 3\cos\theta, \tag{3.5b}$$
$$f_2(\theta) = 4\cos^2\theta - 1, \tag{3.5c}$$

where $\bar{l} = 2\bar{r}/a$.

Similarly, the boundary curve of $\theta_{CD}(\lambda)$ can be determined by geometry analysis on the post arrangement in figure 7(*c*). It denotes that the radius of post 3 reaches its minimum while the other two posts have their maximum radii. The burst occurs for the meniscus connecting posts 2 and 3 and later the two menisci merge into a new one (overlap). Again, based on geometry analysis (§ B.2), we derive the semi-analytical solution for $\theta_{CD}(\lambda)$:

$$\theta_{CD}(\lambda): \quad g_4\Theta^4 + g_3\Theta^3 + g_2\Theta^2 + g_1\Theta + g_0 = 0, \tag{3.6a}$$

with

$$\Theta = \frac{\bar{l}\cos\theta\,(1 - \lambda^2\bar{l}^2) + \sqrt{\lambda^2\bar{l}^4 f_4(\theta) - \bar{l}^2[f_4(\theta) + \lambda^2] + 1}}{2(1 - \lambda^2\bar{l}^2\cos^2\theta)}, \tag{3.6b}$$

$$g_4 = f_3^2(2\theta), \tag{3.6c}$$
$$g_3 = -2f_3(2\theta)f_3(\theta)(1 + \lambda)\bar{l}, \tag{3.6d}$$
$$g_2 = \left[f_3^2(\theta) + \tfrac{1}{2}f_3(2\theta)\right](1 + \lambda)^2\bar{l}^2 - 1, \tag{3.6e}$$
$$g_1 = (1 + \lambda)\bar{l}\left[\cos\theta - \tfrac{1}{2}(1 + \lambda)^2\bar{l}^2 f_3(\theta)\right], \tag{3.6f}$$
$$g_0 = \tfrac{1}{4}(1 + \lambda)^2\bar{l}^2\left[\tfrac{1}{4}(1 + \lambda)^2\bar{l}^2 - 1\right], \tag{3.6g}$$
$$f_3(\theta) = \sqrt{3}\sin\theta + \cos\theta, \tag{3.6h}$$
$$f_4(\theta) = \sin^2\theta + \lambda^2\cos^2\theta. \tag{3.6i}$$

Finally, we derive the analytical (or semi-analytical) solutions of the upper and lower bounds (in terms of contact angle θ) of the cross-over zone for porous media with arbitrary flow geometry at a given disorder λ. As shown in (3.5) and (3.6), only one parameter, $\bar{l} = 2\bar{r}/a$, is included in the theoretical model.

The phase diagram predicted by the theoretical model is also presented in figure 7(*a*), which describes the cross-over from capillary fingering to compact displacement in disordered porous media from weak imbibition ($\theta = 45°$) to strong drainage ($\theta = 180°$). The cross-over zone denoted by the contact angle range of $[\theta_{CD}(\lambda),\ \theta_{CF}(\lambda)]$ expands as the porous medium becomes more disordered, with a
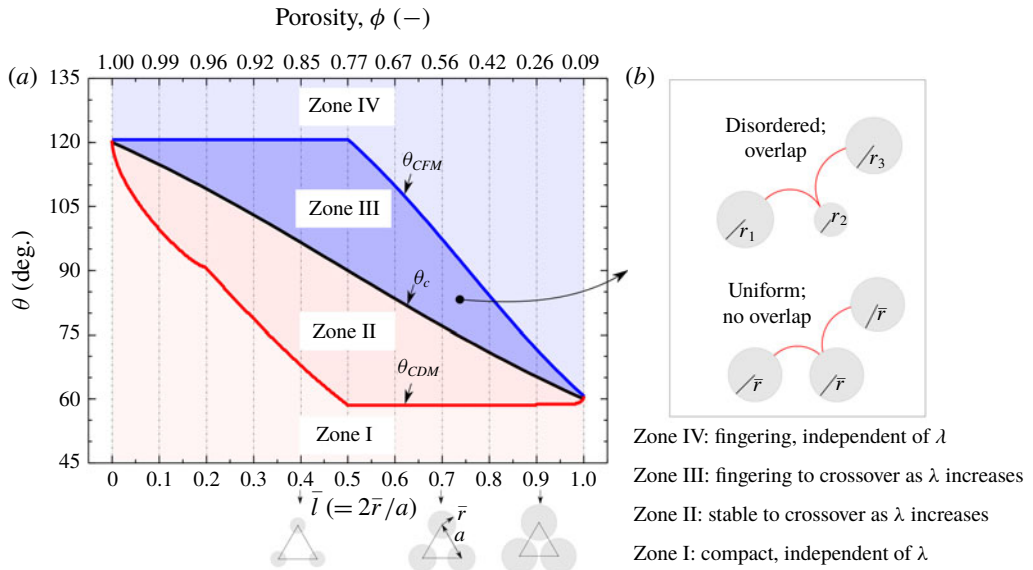
FIGURE 8. (Colour online) The disorder effect on fluid invasion depends not only on contact angle, but also on the compactness represented by $\bar{l}$ or porosity $\phi = 1 - (\pi/(2\sqrt{3}))\bar{l}^2$. (*a*) Four zones are defined in the $\bar{l}$–θ plane. For zone I and zone IV, the displacement patterns are respectively compact and unstable, independent of disorder λ. In zone II, increasing the disorder λ destabilizes the displacement front, and the mechanism is well described by the pore-scale images recorded with microscopy (figure 5). For zone III, increasing the disorder λ stabilizes the displacement front, and the mechanism is shown in panel (*b*).

single point located at the critical contact angle θ_c for uniform porous media and approaching the maximum of $[\theta_{CDM}, \theta_{CFM}]$ at λ_{max}. Here, θ_{CDM} is the minimum of θ_{CD}; θ_{CFM} is the maximum of θ_{CF}; and λ_{max} is the maximum disorder corresponding to the state of post overlapping. The phase diagram also elucidates that the impact of disorder on the displacement pattern depends on the wettability, as further illustrated in figure 8. From figure 8, θ_{CDM}, θ_c and θ_{CFM} vary with the compactness of the porous medium that is represented by $\bar{l}$ $(= 2\bar{r}/a)$ or porosity ϕ $(= 1 - (\pi/(2\sqrt{3}))\bar{l}^2)$, and the critical contact angle θ_c decreases with ϕ or $\bar{r}$, consistent with the previous numerical results (Koiller *et al.* 1992).

Figure 8 further indicates that the wettability-dependent disorder impact on quasi-static displacement can be represented with four zones, i.e. zone I, zone II, zone III and zone IV. For zone I ($\theta < \theta_{CDM}$) and zone IV ($\theta > \theta_{CFM}$), the patterns are respectively compact and unstable, independent of disorder λ. In zone II, increasing the disorder λ destabilizes the displacement front, which has been well investigated in the previous studies (Koiller *et al.* 1992; Yortsos *et al.* 1997; Toussaint *et al.* 2005; Holtzman & Juanes 2010; Xu *et al.* 2014; Holtzman 2016), and the mechanism is well described by the pore-scale images recorded with microscopy (figure 4). For zone III, however, increasing the disorder λ stabilizes the displacement front, and the mechanism is given in figure 8(*b*). In this zone, two competing mechanisms are responsible for the disorder effect. On the one hand, for a given contact angle θ ($\theta_c < \theta < \theta_{CFM}$), burst dominates the fluid displacement, destabilizing the fluid–fluid

interface. On the other hand, as the porous medium becomes more disordered, overlap may occur to stabilize the interface (figure 8*b*). The latter would gradually become a dominant mechanism as λ gradually increases, leading to a stabilizing effect.

Holtzman (2016) also investigated the effect of the disorder on displacement patterns. For the microfluidics in Holtzman (2016), $\bar{l} = 0.54$, and the corresponding θ_c is 87° (obtained from figure 8*a*). The numerical results in Holtzman (2016) showed that, for $\theta = 90°$, i.e. in zone III, increasing disorder would destabilize the displacement front, which is inconsistent with our work. This is attributed to the dynamic effect involved in the study of Holtzman (2016) ($Ca = 1.4 \times 10^{-5}$). The dynamic effect would enhance the number of fingers, destabilize the displacement front, and finally enhance trapping, which is amplified when increasing disorder (Holtzman 2016). In other words, when the capillary force plays a role in multiphase flow, increasing disorder would significantly enhance trapping, which dominates the mechanism shown in figure 8(*b*), and finally destabilizes the displacement front. This destabilizing effect due to the role of viscous force is not considered in this work. Under quasi-static conditions, however, the effect of disorder and wettability can be well captured by the probability of overlap, which will be evaluated via simulations and experimental results shown in § 3.3.3.

3.3.3. *Evaluation*

Given that the pore-scale simulations can generally capture the impact of disorder on the quasi-static displacement as discussed in § 3.1, the pore-scale simulations enable us to evaluate the proposed phase diagram of quasi-static fluid displacement with a larger range of disorder and contact angle that cannot be achieved in microfluidic experiments. We perform pore-scale numerical simulations with $45° \leqslant \theta \leqslant 180°$ and $0 \leqslant \lambda \leqslant 0.4$, and consider 243 points of $[\theta, \lambda]$. For each point, 10 geometries are generated independently. In total, we simulate 2430 computational cases. We evaluate the phase diagram with invading fluid saturation S_{br} and specific fluid–fluid interface length l_{nw} at the time of breakthrough, as presented in figure 9. The dots represent the average values for S_{br} and l_{nw} from the 10 simulated cases. From figure 9(*a*,*b*) we see that the theoretical model (3.5) and (3.6) well predicts the regimes of capillary fingering (figure 9*e*), compact displacement (figure 9*c*) and the cross-over zone (figure 9*d*) in the θ–λ plane. Figure 9(*d*,*e*) also shows the defending fluid trapped within single or multiple pores in disordered porous media, indicating that the numerical method is able to capture the trapping behaviour in multiphase flow.

Based on the simulation results in figure 9, we also present the details of disorder impact on S_{br} and l_{nw} in zone II (figure 10*a*,*b*) and in zone III (figure 10*c*,*d*). As in figure 9, in figure 10, the data points indicate the average values of 10 simulated cases, and the error bars indicate standard deviations. The boundaries separating different displacement patterns predicted by the theoretical model are also presented with vertical lines. In zone II, increasing λ decreases S_{br} and increases l_{nw}, thus destabilizing the displacement front ranging from compact to cross-over at the critical disorder, λ_{CD}. In zone III, conversely, a stabilizing effect can be seen in which, as λ increases, the displacement shifts fingering to cross-over at the critical disorder, λ_{CF}, which supports the results in figure 8. Given that our numerical simulation can describe the trapping during quasi-static immiscible displacement, the consistency between simulations and the theoretical model indicates that the trapping can be reasonably considered when using the probability of overlap to relate displacement patterns, as discussed in §§ 3.2 and 3.3.2. Compared with zone II, however, in
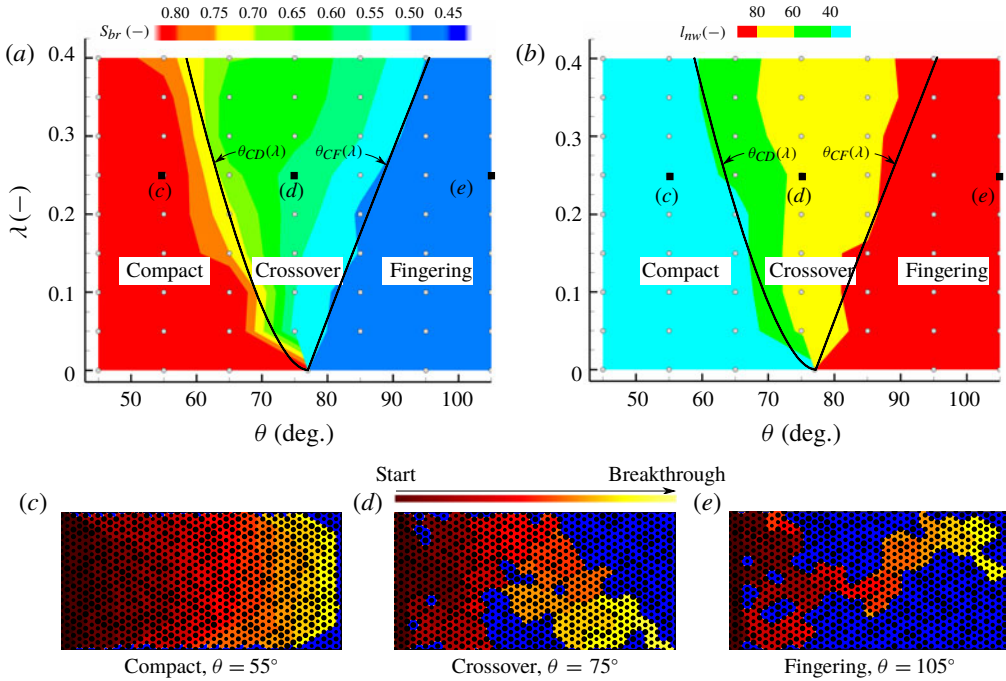
FIGURE 9. (Colour online) Evaluation of the proposed phase diagram with simulated invading fluid saturation S_{br} (*a*) and specific fluid–fluid interface length l_{nw} (*b*) at the time of breakthrough. The dots represent the average values for S_{br} and l_{nw} from 10 simulated cases. These 10 geometries are generated independently at a given disorder λ. The theoretical model predicts the cross-over from capillary fingering to compact displacement, and the representative fluid invasion morphologies are shown in (*c*) compact displacement, (*d*) cross-over and (*e*) capillary fingering. In (*c–e*), to show the evolution of displacement front, the dark red represents the initial stage whereas the light red indicates the late time.

zone III, we observe that the variations of S_{br} and l_{nw} are insensitive to the change in λ, and thus we can conclude that the impact of disorder on displacement patterns is less significant for $\theta_c < \theta < \theta_{CFM}$. Figure 10(*e*,*f*) confirms that increasing θ decreases S_{br} and increases l_{nw} for a porous medium with a given λ, thus destabilizing the displacement from compact to cross-over to capillary fingering (Jung *et al.* 2016; Hu *et al.* 2018*a*; Primkulov *et al.* 2018). The two critical contact angles θ_{CD} and θ_{CF} predicted by the theoretical model well capture the boundaries among these three flow regimes.

We also evaluate the phase diagram using experimental results. The experiments in microfluidics with different disorders under different wetting conditions are quite limited. Here, the experimental results in this work and the experiments conducted by Jung *et al.* (2016) are employed to evaluate the proposed phase diagram. Given that one parameter ($\bar{l} = 2\bar{r}/a$) is involved in the theoretical model ($\theta_{CF}(\lambda)$ and $\theta_{CD}(\lambda)$), the parameter $\bar{l}$ needs to be determined. In this work, $a = 250$ µm, $\bar{r} = 78.5$ µm and hence $\bar{l} = 0.628$. The theoretical model is then presented in figure 11(*a*), which is able to well capture the observed displacement patterns of cross-over (open circles) and compact displacement (solid circles), respectively. We also present the boundary curves for the four specific geometries (previously shown in figure 6*a*) in figure 11(*a*), demonstrating that the cross-over zone determined via specific geometries is included
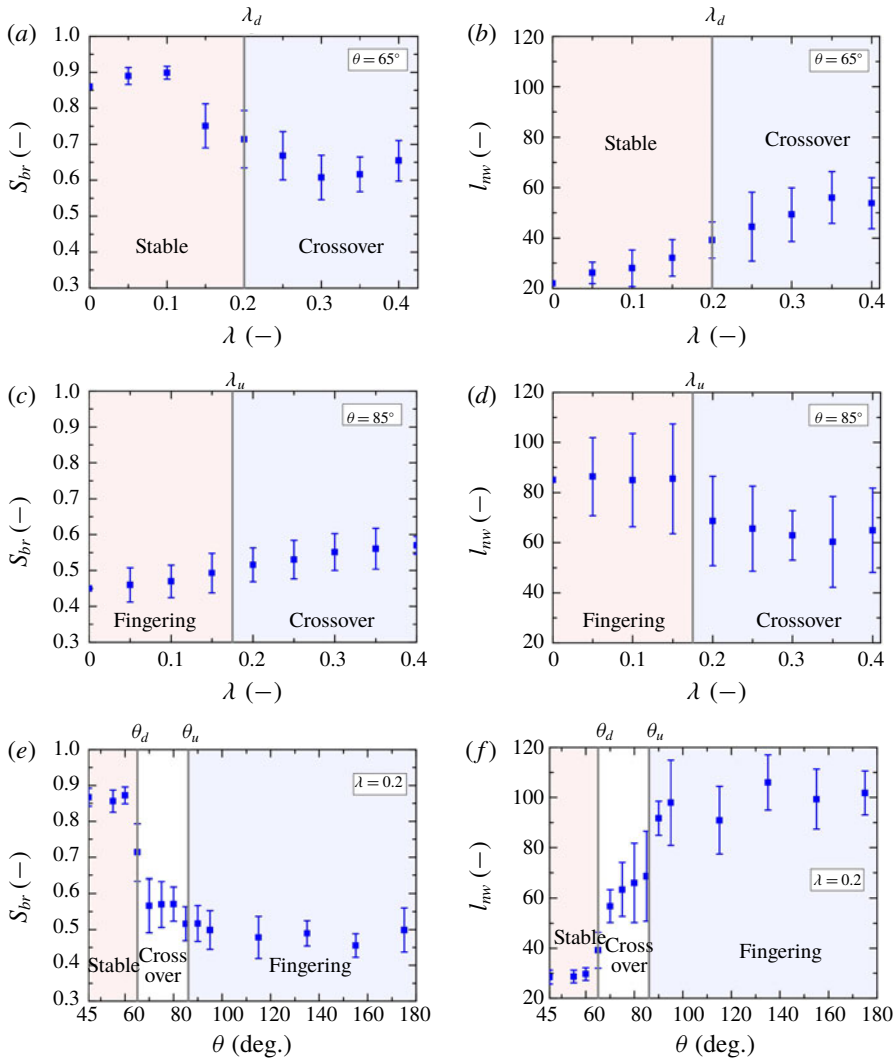
FIGURE 10. (Colour online) Variations of invading fluid saturation S_{br} (*a,c,e*) and specific fluid–fluid interface length l_{nw} (*b,d,f*) with λ in zone II (*a,b*), i.e. $\theta_{CDM} < \theta = 65° < \theta_c$, with λ in zone III (*c,d*), i.e. $\theta_c < \theta = 85° < \theta_{CFM}$, and with θ for $45° < \theta < 180°$ at $\lambda = 0.2$ (*e,f*). The data points (squares) indicate the average values of 10 simulated cases, and the error bars indicate standard deviations. The boundaries separating different displacement patterns predicted by the theoretical model are also presented with vertical lines. (*a,b*) In zone II, increasing λ decreases S_{br} and increases l_{nw}, thus destabilizing the displacement front ranging from compact to cross-over at λ_{CD}. (*c,d*) In zone III, a stabilizing effect is observed. The variations of S_{br} and l_{nw} are insensitive to the change in λ, indicating that the impact of disorder on the displacement pattern is less significant. (*e,f*) Increasing θ decreases S_{br} and increases l_{nw} at $\lambda = 0.2$, thus destabilizing the displacement front, which shifts from compact to cross-over to capillary fingering. The two critical contact angles θ_{CD} and θ_{CF} separate these three flow regimes.
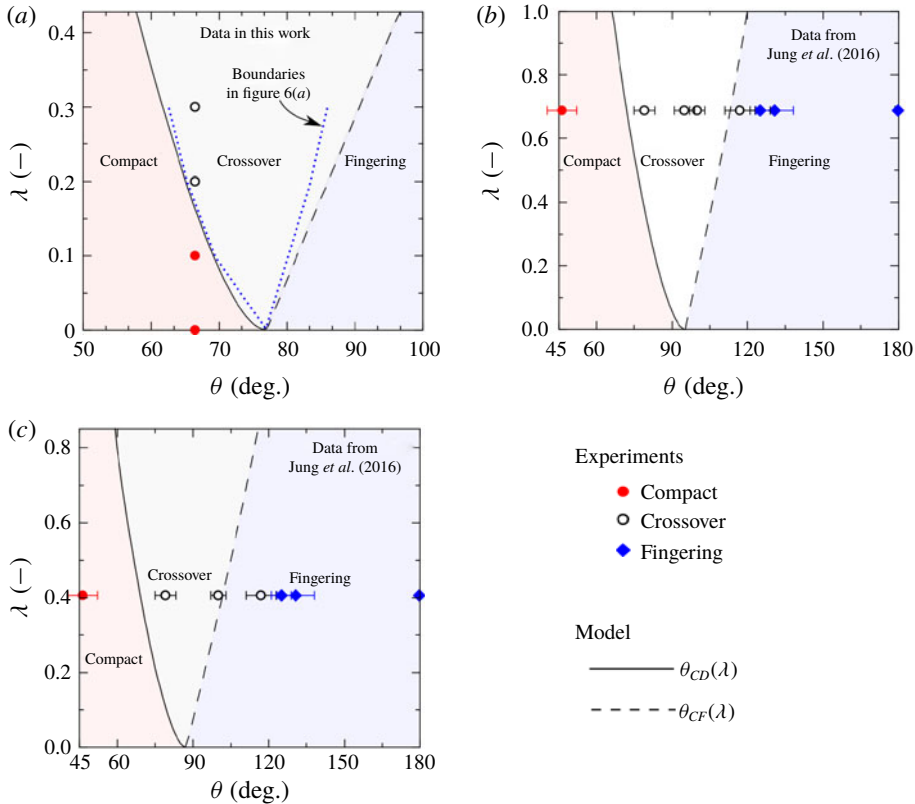
FIGURE 11. (Colour online) Evaluation of phase diagram using the experimental results in this work and the experiments by Jung *et al.* (2016). In this work, $\bar{l} = 0.7$ and $\theta = 67°$, and the theoretical model is then presented in (*a*), which is able to well capture the observed displacement patterns of cross-over (open circles) and compact displacement (solid circles), respectively. (*b*) In the experiments of Jung *et al.* (2016) with porosity $\phi = 0.85$, the theoretical model predicts well the cross-over from the capillary fingering to compact displacement as θ decreases from 150° to 45°. (*c*) A microfluidic experiment with $\phi = 0.7$ is also adopted herein. The cross-over from fingering to compact displacement is also captured by the theoretical model. In (*b*,*c*), the horizontal bars indicate standard deviations of contact angle measurements.

in the cross-over zone predicted by the theoretical model. This is because the boundary curves of θ_{CDM} and θ_{CFM} represent the lower and upper bounds for the cross-over zone for an arbitrary geometry with a given disorder. Jung *et al.* (2016) conducted slow immiscible displacement in disordered microfluidics to investigate the wettability effect. For the microfluidics with porosity $\phi = 0.85$, $r = \bar{r} = 16$ μm and 21 μm $\leqslant d \leqslant$ 65 μm, the parameter $\bar{l}$ can be estimated with $\phi = 1 - (\pi/2\sqrt{3})\bar{l}^2 = 0.4067$ and the disorder λ is determined as $\lambda = (d_{max} - d_{min})/(4\bar{r}) = 0.6875$. As shown in figure 11(*b*), the theoretical model predicts well the cross-over from capillary fingering to compact displacement as θ decreases from 150° to 45°. For another microfluidic with $\phi = 0.7$ (figure 11*c*), $r = \bar{r} = 16$ μm and 14 μm $\leqslant d \leqslant 40$ μm, $\bar{l}$ is determined as 0.5751 and $\lambda = (d_{max} - d_{min})/(4\bar{r}) = 0.4063$. The theoretical model again captures well the cross-over from fingering to compact displacement for a given disorder.

4. Conclusions

We study the competing effect of disorder and wettability on the quasi-static fluid displacement in porous media by combining microfluidic experiments and pore-scale simulations with theoretical analysis. Through microfluidic experiments, we show that increasing disorder destabilizes the invasion morphologies at weak imbibition and the underlying mechanism at the pore scale can be well recorded with the microscope. We develop the numerical method originally proposed by Cieplak & Robbins (1988, 1990) to consider the rectangular domain with constant-flow-rate boundaries to match the experimental conditions. Numerical simulations generally agree with the experimental results, and thus the numerical method can be employed to systematically investigate the quasi-static fluid displacement in porous media with different disorders and contact angles that cannot be achieved in microfluidic experiments.

Through theoretical analysis on the probability of overlap events that stabilize the fluid–fluid interface, we propose a theoretical model to describe the lower and upper bounds of cross-over between capillary fingering and compact displacement in porous media with a given disorder. The phase diagram predicted by the theoretical model not only captures the boundaries that separate the regimes but also identifies four zones to elucidate that the impact of disorder depends on contact angle. In zone II ($\theta_{CDM} < \theta < \theta_c$), increasing λ destabilizes the displacement patterns, and the underlying mechanism is well explained by the pore-scale images recorded with the microscope. For zone III ($\theta_c < \theta < \theta_{CFM}$), however, we show that a stabilizing effect of disorder plays a role because the non-uniform posts would stabilize the local fluid–fluid interface. We find that this destabilizing effect is less significant than that in zone II. In zone I and zone IV, displacement patterns respectively exhibit compact displacement and capillary fingering, independent of both contact angle and disorder. Finally, the proposed phase diagram is evaluated using the extensive pore-scale simulations, and the experimental results in this work and in the literature.

Our proposed phase diagram, different from the previous works that consider the flow rate, the wetting condition and the fluid properties (Lenormand *et al.* 1988; Holtzman & Juanes 2010; Zhang *et al.* 2011), defines the lower and upper bounds of the cross-over zone between compact displacement and capillary fingering for an arbitrary flow geometry with a given disorder. Thus, our work extends the previous studies to consider the impact of flow geometry. The proposed phase diagram provides the first identification of displacement patterns just using the statistical parameters such as porosity, average particle/pore sizes and disorder. Thus, our work is of practical significance for engineering applications, such as geological carbon sequestration, oil recovery and shale gas production, where the identification of the displacement pattern is critical for controlling the hydraulic properties of the multiphase flow system in order to ensure recovery efficiency. Note that in this work we only consider triangular lattice packing and uniform post size distribution for a fixed porosity and a fixed correlation length. Many geologic media often have an intrinsic spatial correlation and do not follow a uniform pore size distribution (or do not exhibit triangular lattice packing). The system size of the flow geometry is also fixed as 10 mm × 5 mm (including 987 posts) in this work, and the system size may also affect the displacement, which is not considered in this work. Thus, the impacts of the spatial correlation length (Holtzman 2016; Borgman *et al.* 2019), the distribution type, the post packing and the system size on the multiphase flow need further investigation to improve the generality of the theoretical model. Another important open question is to extend the proposed phase diagram from weak imbibition to strong imbibition in which corner flow plays a key role in quasi-static displacement (Girardo *et al.* 2009; Primkulov *et al.* 2018).

Appendix A. The occurrence of three basic modes

A.1. *Burst*

As shown in figure 2(a), for a three-post arrangement, the arc touches the posts O_1 and O_2 at B and C, and the radius of curvature is $R = \overline{AB} = \overline{AC}$. Note that because $\angle DBO_1 = \angle ABE = 90°$, we have $\angle ABO_1 = \angle DBE = \theta$ and similarly $\angle ACO_2 = \theta$. Applying the law of cosines in $\triangle AO_1B$ and $\triangle AO_2C$, we have

$$\left.\begin{aligned} y_1^2 &= r_1^2 + R^2 - 2r_1 R \cos\theta, \\ y_2^2 &= r_2^2 + R^2 - 2r_2 R \cos\theta, \end{aligned}\right\} \tag{A 1}$$

where R is the radius of curvature of the arc. The radius R increases with y_1 and y_2. The radius R reaches its minimum (R_b) corresponding to the condition that $y_1 + y_2$ also reaches its minimum. In the post arrangement shown in figure 2(a), the minimum of $y_1 + y_2$ means that the point A lies on the line O_1O_2, i.e. $y_1 + y_2 = a$. Substituting $y_1 + y_2 = a$ into (A 1), we can obtain the critical radius of curvature for the burst mode as

$$\text{burst:}\quad R_b = \frac{-b_1 + \sqrt{b_1^2 - 4a_1 c_1}}{2a_1}, \tag{A 2}$$

with

$$\left.\begin{aligned} a_1 &= \frac{2}{a^2}(r_1 - r_2)^2 \cos^2\theta - 2, \\ b_1 &= 2(r_1 + r_2)\cos\theta - \frac{2}{a^2}(r_1 - r_2)^2(r_1 + r_2)\cos\theta, \\ c_1 &= \frac{a^2}{2} + \frac{1}{2a^2}(r_1^2 - r_2^2)^2 - r_1^2 - r_2^2, \end{aligned}\right\} \tag{A 3}$$

where r_1 and r_2 are the radii of post 1 and post 2, and θ is the invading fluid contact angle.

A.2. *Touch*

As shown in figure 2(b), again, applying the law of cosines in $\triangle AO_1B$, $\triangle AO_2C$, $\triangle AO_1O_3$ and $\triangle AO_2O_3$, we have

$$\left.\begin{aligned} y_1^2 &= r_1^2 + R_t^2 - 2r_1 R_t \cos\theta, \\ y_2^2 &= r_2^2 + R_t^2 - 2r_2 R_t \cos\theta, \\ y_1^2 &= a^2 + (R_t + r_3)^2 - 2a(R_t + r_3)\cos\gamma, \\ y_2^2 &= a^2 + (R_t + r_3)^2 - 2a(R_t + r_3)\cos(60° - \gamma). \end{aligned}\right\} \tag{A 4}$$

From (A 4), we can obtain the analytical solution of the critical radius of curvature, R_t, for the touch mode as

$$\text{touch:}\quad R_t = \frac{-b_2 + \sqrt{b_2^2 - 4a_2 c_2}}{2a_2}, \tag{A 5}$$

with

$$a_2 = 4r_3^2 + 4\cos^2\theta\,(r_1^2 + r_2^2 - 4r_1 r_3) + 4r_3\cos\theta\,(r_2 + r_1) - 3a^2,$$
$$b_2 = 2a^2(r_1\cos\theta + r_2\cos\theta - 2r_3) + 2r_1\cos\theta\,(r_2^2 + r_3^2 - 2r_1^2)$$
$$\qquad + 2r_2\cos\theta\,(r_1^2 + r_3^2 - 2r_2^2) + 2r_3(2r_3^2 - r_1^2 - r_2^2),$$
$$c_2 = a^2(a^2 - r_1^2 - r_2^2 - r_3^2) + \tfrac{1}{2}(r_1^2 - r_2^2)^2 + \tfrac{1}{2}(r_1^2 - r_3^2)^2 + \tfrac{1}{2}(r_2^2 - r_3^2)^2. \tag{A 6}$$

A.3. *Overlap*

As shown in figure 2(d), the overlap will occur if $\eta_2 + \eta_3 \geqslant \angle O_1 O_2 O_3$. Similar to the procedures given in (A 2) and (A 5), applying the law of cosines in $\triangle AO_1 B$ and $\triangle AO_2 C$, we have

$$y_1^2 = r_1^2 + R^2 - 2r_1 R\cos\theta,$$
$$y_2^2 = r_2^2 + R^2 - 2r_2 R\cos\theta, \tag{A 7}$$

and the law of sines in $\triangle AO_2 C$ leads to

$$\frac{y_2}{\sin\theta} = \frac{R}{\sin\alpha_2}. \tag{A 8}$$

By the above two equations, the expression for α_2 can be written as

$$\cos\alpha_2 = \frac{r_2 - R\cos\theta}{\sqrt{r_2^2 + R^2 - 2r_2 R\cos\theta}}. \tag{A 9}$$

The expression for β_2 can also be obtained via the law of cosines in $\triangle AO_1 O_2$, $\triangle AO_1 B$ and $\triangle AO_2 C$,

$$\cos\beta_2 = \frac{a^2 + r_2^2 - r_1^2 + 2(r_1 - r_2)\cos\theta}{2a\sqrt{r_2^2 + R^2 - 2r_2 R\cos\theta}}. \tag{A 10}$$

By (A 9) and (A 10), the angle of η_2 and η_3 can be written as

$$\eta_2 = \cos^{-1}\left(\frac{r_2 - R\cos\theta}{\sqrt{r_2^2 + R^2 - 2r_2 R\cos\theta}}\right) - \cos^{-1}\left(\frac{a^2 + r_2^2 - r_1^2 + 2(r_1 - r_2)\cos\theta}{2a\sqrt{r_2^2 + R^2 - 2r_2 R\cos\theta}}\right). \tag{A 11}$$

Similarly, the angle of η_2 can also be expressed as

$$\eta_3 = \cos^{-1}\left(\frac{r_2 - R\cos\theta}{\sqrt{r_2^2 + R^2 - 2r_2 R\cos\theta}}\right) - \cos^{-1}\left(\frac{a^2 + r_2^2 - r_3^2 + 2(r_3 - r_2)\cos\theta}{2a\sqrt{r_2^2 + R^2 - 2r_2 R\cos\theta}}\right). \tag{A 12}$$

Appendix B. The derivation of the theoretical model

B.1. *The derivation of* $\theta_{CF}(\lambda)$

For $\theta_{CF}(\lambda)$, as shown in figure 7(d), the three radii reach their minimum, i.e. $r_1 = r_2 = r_3 = (1 - \lambda)\bar{r}$, and the burst occurs for the two menisci. Based on (A 9), with $\angle AO_2 C = 60°$, we have

$$\cos 60° = \frac{(1 - \lambda)\bar{r} - R_b\cos\theta}{\sqrt{R_b^2 + (1 - \lambda)^2\bar{r}^2 - 2(1 - \lambda)\bar{r}R_b\cos\theta}}. \tag{B 1}$$

From (B 1), R_b can be solved as

$$R_b = \frac{\sqrt{3}\sin\theta - 3\cos\theta}{1 - 4\cos^2\theta}(1 - \lambda)\bar{r}. \tag{B 2}$$

For the burst mode, the critical radius of curvature is expressed by (A 2), and substituting $r_1 = r_2 = r_3 = (1 - \lambda)\bar{r}$ into (A 2) leads to

$$R_b = \tfrac{1}{2}\sqrt{a^2 - [2(1 - \lambda)\bar{r}]^2\sin^2\theta} + (1 - \lambda)\bar{r}\cos\theta. \tag{B 3}$$

Combining (B 2) with (B 3), we derive the analytical solution for $\theta_{CF}(\lambda)$, as given in (3.5).

B.2. *The derivation of $\theta_{CD}(\lambda)$*

For $\theta_{CD}(\lambda)$, as shown in figure 7(*c*), the radius of post 3 reaches its minimum, i.e. $r_3 = (1 - \lambda)\bar{r}$, while the other two posts reach their maximum radii, i.e. $r_1 = r_2 = (1 + \lambda)\bar{r}$. The burst occurs for the meniscus connecting posts 2 and 3 and later the two menisci merge into a single one (overlap). Again, for the burst, the critical radius of curvature is expressed by (A 2), and substituting $r_3 = (1 - \lambda)\bar{r}$ and $r_2 = (1 + \lambda)\bar{r}$ into (A 2) leads to

$$R_b = \frac{2\bar{r}\cos\theta\,(a^2 - 4\lambda^2\bar{r}^2) + a\sqrt{\left(\begin{array}{c}16\lambda^2\bar{r}^4[\sin^2\theta + \lambda^2\cos^2\theta]\\ -4a^2\bar{r}^2(\sin^2\theta + \lambda^2 + \lambda^2\cos^2\theta) + a^4\end{array}\right)}}{2(a^2 - 4\lambda^2\bar{r}^2\cos^2\theta)}. \tag{B 4}$$

From the geometry shown in figure 7(*c*), we have

$$2\alpha - \beta = 120°, \quad \cos\beta = \frac{a}{2y}, \quad \sin\alpha = \frac{R_b\sin\theta}{y}. \tag{B 5a–c}$$

By (A 9), $\cos\alpha$ is written as

$$\cos\alpha = \frac{(1 + \lambda)\bar{r} - R_b\cos\theta}{y}. \tag{B 6}$$

Using trigonometric functions, we have

$$\sin 2\alpha = 2\sin\alpha\cos\alpha = 2R_b\sin\theta[(1 + \lambda)\bar{r} - R_b\cos\theta]/y^2, \tag{B 7}$$

$$\cos 2\alpha = \cos^2\alpha - \sin^2\alpha = \frac{R_b^2(\cos^2\theta - \sin^2\theta) - 2R_b(1 + \lambda)\bar{r}\cos\theta + (1 + \lambda)^2\bar{r}^2}{2y^2}, \tag{B 8}$$

$$\cos\beta = \cos(2\alpha - 120°) = -\tfrac{1}{2}\cos 2\alpha + \tfrac{\sqrt{3}}{2}\sin 2\alpha. \tag{B 9}$$

Substituting (B 5), (B 7) and (B 8) into (B 9) leads to

$$ay = -(\sqrt{3}\sin 2\theta + \cos 2\theta)R_b^2 + 2(\sqrt{3}\sin\theta + \cos\theta)(1 + \lambda)\bar{r}R_b - (1 + \lambda)^2\bar{r}^2. \tag{B 10}$$

Applying the law of cosines in $\triangle AO_2C$ provides the relation between R_b and y,

$$y^2 = (1 + \lambda)^2\bar{r}^2 + R_b^2 - 2(1 + \lambda)\bar{r}R_b\cos\theta. \tag{B 11}$$

Finally, the boundary curve $\theta_{CD}(\lambda)$ can be determined via the combination of (B 4), (B 10) and (B 11), as rearranged in (3.6).

REFERENCES

ALAVA, M., DUBÉ, M. & ROST, M. 2004 Imbibition in disordered media. *Adv. Phys.* **53** (2), 83–175.

ANDERSON, R., ZHANG, L. & DING, Y. 2010 A critical review of two-phase flow in gas flow channels of proton exchange membrane fuel cells. *J. Power Sources* **195** (15), 4531–4553.

ARMSTRONG, R. T. & BERG, S. 2013 Interfacial velocities and capillary pressure gradients during Haines jumps. *Phys. Rev.* E **88** (4), 043010.

BABCHIN, A., BRAILOVSKY, I., GORDON, P. & SIVASHINSKY, G. 2008 Fingering instability in immiscible displacement. *Phys. Rev.* E **77** (2), 026301.

BACHU, S. 2015 Review of CO_2 storage efficiency in deep saline aquifers. *Intl J. Greenh. Gas Control* **40**, 188–202.

BENSON, S. M. & COLE, D. R. 2008 CO_2 sequestration in deep sedimentary formations. *Elements* **4** (5), 325–331.

BERG, S., OTT, H., KLAPP, S. A., SCHWING, A., NEITELER, R., BRUSSEE, N., MAKURAT, A., LEU, L., ENZMANN, F., SCHWARZ, J. O. *et al.* 2013 Real-time 3D imaging of Haines jumps in porous media flow. *Proc. Natl Acad. Sci. USA* **110** (10), 3755–3759.

BISCHOFBERGER, I., RAMACHANDRAN, R. & NAGEL, S. R. 2014 Fingering versus stability in the limit of zero interfacial tension. *Nat. Commun.* **5**, 5265.

BORGMAN, O., DARWENT, T., SEGRE, E., GOEHRING, L. & HOLTZMAN, R. 2019 Immiscible fluid displacement in porous media with spatially correlated particle sizes. *Adv. Water Resour.* **128**, 158–167.

BORGMAN, O., FANTINEL, P., LÜHDER, W., GOEHRING, L. & HOLTZMAN, R. 2017 Impact of spatially correlated pore-scale heterogeneity on drying porous media. *Water Resour. Res.* **53** (7), 5645–5658.

CHAPUIS, O., PRAT, M., QUINTARD, M., CHANE-KANE, E., GUILLOT, O. & MAYER, N. 2008 Two-phase flow and evaporation in model fibrous media. *J. Power Sources* **178** (1), 258–268.

CHAUDHARY, K., CARDENAS, M. B., WOLFE, W. W., MAISANO, J. A., KETCHAM, R. A. & BENNETT, P. C. 2013 Pore-scale trapping of supercritical CO_2 and the role of grain wettability and shape. *Geophys. Res. Lett.* **40** (15), 3878–3882.

CHEN, J. D. & WILKINSON, D. 1985 Pore-scale viscous fingering in porous media. *Phys. Rev. Lett.* **55** (18), 1892–1895.

CHEN, Y.-F., FANG, S., WU, D.-S. & HU, R. 2017 Visualizing and quantifying the crossover from capillary fingering to viscous fingering in a rough fracture. *Water Resour. Res.* **53** (9), 7756–7772.

CHEN, Y.-F., WU, D.-S., FANG, S. & HU, R. 2018 Experimental study on two-phase flow in rough fracture: phase diagram and localized flow channel. *Intl J. Heat Mass Transfer* **122**, 1298–1307.

CIEPLAK, M. & ROBBINS, M. O. 1988 Dynamical transition in quasistatic fluid invasion in porous media. *Phys. Rev. Lett.* **60** (20), 2042–2045.

CIEPLAK, M. & ROBBINS, M. O. 1990 Influence of contact angle on quasistatic fluid invasion of porous media. *Phys. Rev.* B **41** (16), 11508.

CONCUS, P. & FINN, R. 1969 On the behavior of a capillary surface in a wedge. *Proc. Natl Acad. Sci. USA* **63** (2), 292.

COTTIN, C., BODIGUEL, H. & COLIN, A. 2011 Influence of wetting conditions on drainage in porous media: a microfluidic study. *Phys. Rev.* E **84** (2), 026311.

DAWSON, H. E. & ROBERTS, P. V. 1997 Influence of viscous, gravitational, and capillary forces on dnapl saturation. *Ground Water* **35** (2), 261–269.

DONG, M. & CHATZIS, I. 1995 The imbibition and flow of a wetting liquid along the corners of a square capillary tube. *J. Colloid Interface Sci.* **172** (2), 278–288.

DVRAAM, D. G. & PAYATAKES, A. C. 1995 Flow regimes and relative permeabilities during steady-state two-phase flow in porous media. *J. Fluid Mech.* **293**, 207–236.

FERRARI, A., JIMENEZ-MARTINEZ, J., BORGNE, T. L., MÉHEUST, Y. & LUNATI, I. 2015 Challenges in modeling unstable two-phase flow experiments in porous micromodels. *Water Resour. Res.* **51** (3), 1381–1400.

GEISTLINGER, H., ATAEI-DADAVI, I., MOHAMMADIAN, S. & VOGEL, H. J. 2015 The impact of pore structure and surface roughness on capillary trapping for 2-D and 3-D porous media. *Water Resour. Res.* **51**, 9094–9111.

GIRARDO, S., CINGOLANI, R., CHIBBARO, S., DIOTALLEVI, F., SUCCI, S. & PISIGNANO, D. 2009 Corner liquid imbibition during capillary penetration in lithographically made microchannels. *Appl. Phys. Lett.* **94** (17), 171901.

HECHT, I. & TAITELBAUM, H. 2004 Roughness and growth in a continuous fluid invasion model. *Phys. Rev.* E **70** (4), 046307.

HOLTZMAN, R. 2016 Effects of pore-scale disorder on fluid displacement in partially-wettable porous media. *Sci. Rep.* **6**, 36221.

HOLTZMAN, R. & JUANES, R. 2010 Crossover from fingering to fracturing in deformable disordered media. *Phys. Rev.* E **82** (4), 046305.

HOLTZMAN, R. & SEGRE, E. 2015 Wettability stabilizes fluid invasion into porous media via nonlocal, cooperative pore filling. *Phys. Rev. Lett.* **115** (16), 164501.

HU, R., WAN, J., KIM, Y. & TOKUNAGA, T. K. 2017a Wettability effects on supercritical CO_2cbrine immiscible displacement during drainage: pore-scale observation and 3D simulation. *Intl J. Greenh. Gas Control* **60**, 129–139.

HU, R., WAN, J., KIM, Y. & TOKUNAGA, T. K. 2017b Wettability impact on supercritical CO_2 capillary trapping: pore-scale visualization and quantification. *Water Resour. Res.* **53** (8), 6377–6394.

HU, R., WAN, J., YANG, Z., CHEN, Y.-F. & TOKUNAGA, T. 2018a Wettability and flow rate impacts on immiscible displacement: a theoretical model. *Geophys. Res. Lett.* **45** (7), 3077–3086.

HU, R., WU, D.-S., YANG, Z. & CHEN, Y.-F. 2018b Energy conversion reveals regime transition of imbibition in a rough fracture. *Geophys. Res. Lett.* **45** (7), 8993–9002.

JUNG, M., BRINKMANN, M., SEEMANN, R., HILLER, T., SANCHEZ DE LA LAMA, M. & HERMINGHAUS, S. 2016 Wettability controls slow immiscible displacement through local interfacial instabilities. *Phys. Rev. Fluids* **1** (7), 074202.

KING, P. R. 1987 The fractal nature of viscous fingering in porous media. *J. Phys.* A*: Math. Gen.* **20** (8), L529.

KOILLER, B., JI, H. & ROBBINS, M. O. 1992 Fluid wetting properties and the invasion of square networks. *Phys. Rev.* B **45** (14), 7762–7767.

LEE, H., GUPTA, A., HATTON, T. A. & DOYLE, P. S. 2017 Creating isolated liquid compartments using photopatterned obstacles in microfluidics. *Phys. Rev.* A **7** (4), 044013.

LENORMAND, R., TOUBOUL, E. & ZARCONE, C. 1988 Numerical models and experiments on immiscible displacements in porous media. *J. Fluid Mech.* **189**, 165–187.

LENORMAND, R., ZARCONE, C. & SARR, A. 1983 Mechanisms of the displacement of one fluid by another in a network of capillary ducts. *J. Fluid Mech.* **135**, 337–353.

LEVACHÉ, B. & BARTOLO, D. 2014 Revisiting the Saffman–Taylor experiment: imbibition patterns and liquid-entrainment transitions. *Phys. Rev. Lett.* **113** (4), 044501.

LIU, H., JU, Y., WANG, N., XI, G. & ZHANG, Y. 2015a Lattice Boltzmann modeling of contact angle and its hysteresis in two-phase flow with large viscosity difference. *Phys. Rev.* E **92** (3), 033306.

LIU, H., ZHANG, Y. & VALOCCHI, A. J. 2015b Lattice Boltzmann simulation of immiscible fluid displacement in porous media: homogeneous versus heterogeneous pore network. *Phys. Fluids* **27** (5), 052103.

MÅLØY, K. J., FEDER, J. & JØSSANG, T. 1985 Viscous fingering fractals in porous media. *Phys. Rev. Lett.* **55** (24), 2688.

MORROW, N. R. & MASON, G. 2001 Recovery of oil by spontaneous imbibition. *Curr. Opin. Colloid Interface Sci.* **6** (4), 321–337.

ODIER, C., LEVACHÉ, B., SANTANACH-CARRERAS, E. & BARTOLO, D. 2017 Forced imbibition in porous media: a fourfold scenario. *Phys. Rev. Lett.* **119** (20), 208005.

PATERSON, L. 1981 Radial fingering in a Hele Shaw cell. *J. Fluid Mech.* **113**, 513–529.

PRIMKULOV, B. K., TALMAN, S., KHALEGHI, K., RANGRIZ SHOKRI, A., CHALATURNYK, R., ZHAO, B., MACMINN, C. W. & JUANES, R. 2018 Quasistatic fluid–fluid displacement in porous media: invasion-percolation through a wetting transition. *Phys. Rev. Fluids* **3** (10), 104001.

RABBANI, H. S., OR, D., LIU, Y., LAI, C. Y., LU, N. B., DATTA, S. S., STONE, H. A. & SHOKRI, N. 2018 Suppressing viscous fingering in structured porous media. *Proc. Natl Acad. Sci. USA* **115** (19), 4833–4838.

RAEINI, A. Q., BIJELJIC, B. & BLUNT, M. J. 2015 Modelling capillary trapping using finite-volume simulation of two-phase flow directly on micro-CT images. *Adv. Water Resour.* **83**, 102–110.

ROOF, J. G. 1970 Snap-off of oil droplets in water-wet pores. *SPE J.* **10** (01), 85–90.

SAFFMAN, P. G. & TAYLOR, G. 1958 The penetration of a fluid into a porous medium or Hele-Shaw cell containing a more viscous liquid. *Proc. R. Soc. Lond.* A **245**, 312–329.

SINGH, K., JUNG, M., BRINKMANN, M. & SEEMANN, R. 2019 Capillary-dominated fluid displacement in porous media. *Annu. Rev. Fluid Mech.* **51**, 429–449.

SINGH, K., SCHOLL, H., BRINKMANN, M., MICHIEL, M. D., SCHEEL, M., HERMINGHAUS, S. & SEEMANN, R. 2017 The role of local instabilities in fluid invasion into permeable media. *Sci. Rep.* **7**, 444.

TOUSSAINT, R., LØVOLL, G., MÉHEUST, Y., MÅLØY, K. J. & SCHMITTBUHL, J. 2005 Influence of pore-scale disorder on viscous fingering during drainage. *Eur. Phys. Lett.* **71** (4), 583–589.

TROJER, M., SZULCZEWSKI, M. L. & JUANES, R. 2015 Stabilizing fluid–fluid displacements in porous media through wettability alteration. *Phys. Rev. Appl.* **3**, 054008.

VAN'T VELD, K. & PHILLIPS, O. R. 2010 The economics of enhanced oil recovery: estimating incremental oil supply and CO_2 demand in the Powder River basin. *Energy J.* **31** (4), 31–55.

WANG, Y., ZHANG, C., WEI, N., OOSTROM, M., WIETSMA, T. W., LI, X. & BONNEVILLE, A. 2012 Experimental study of crossover from capillary to viscous fingering for supercritical CO_2 water displacement in a homogeneous pore network. *Environ. Sci. Technol.* **47** (1), 212–218.

WANG, Z., CHAUHAN, K., PEREIRA, J.-M. & GAN, Y. 2019 Disorder characterization of porous media and its effect on fluid displacement. *Phys. Rev. Fluids* **4**, 034305.

WEISLOGEL, M. M. & LICHTER, S. 1998 Capillary flow in an interior corner. *J. Fluid Mech.* **373**, 349–378.

XU, W., OK, J. T., XIAO, F., NEEVES, K. B. & YIN, X. 2014 Effect of pore geometry and interfacial tension on water–oil displacement efficiency in oil-wet microfluidic porous media analogs. *Phys. Fluids* **26** (9), 093102.

YORTSOS, Y. C., XU, B. & SALIN, D. 1997 Phase diagram of fully developed drainage in porous media. *Phys. Rev. Lett.* **79** (23), 4581–4584.

ZACHAROUDIOU, I., CHAPMAN, E. M., BOEK, E. S. & CRAWSHAW, J. P. 2017 Pore-filling events in single junction micro-models with corresponding lattice Boltzmann simulations. *J. Fluid Mech.* **824**, 550–573.

ZHANG, C., OOSTROM, M., WIETSMA, T. W., GRATE, J. W. & WARNER, M. G. 2011 Influence of viscous and capillary forces on immiscible fluid displacement: pore-scale experimental study in a water-wet micromodel demonstrating viscous and capillary fingering. *Energy Fuels* **25** (8), 3493–3505.

ZHAO, B., MACMINN, C. W. & JUANES, R. 2016 Wettability control on multiphase flow in patterned microfluidics. *Proc. Natl Acad. Sci. USA* **113** (37), 10251–10256.